

THE UNIVERSITY OF MANITOBA

MEASUREMENTS OF PROTON TOTAL REACTION CROSS SECTIONS
FOR NICKEL-58, NICKEL-60 AND CALCIUM-48 BETWEEN
22 AND 48 MeV.

by
TIJEN ELIYAKUT

A THESIS
SUBMITTED TO THE FACULTY OF GRADUATE STUDIES
IN PARTIAL FULFILLMENT OF THE REQUIREMENTS FOR
THE DEGREE OF MASTER OF SCIENCE

DEPARTMENT OF PHYSICS



WINNIPEG, MANITOBA

1986

Permission has been granted to the National Library of Canada to microfilm this thesis and to lend or sell copies of the film.

The author (copyright owner) has reserved other publication rights, and neither the thesis nor extensive extracts from it may be printed or otherwise reproduced without his/her written permission.

L'autorisation a été accordée à la Bibliothèque nationale du Canada de microfilmer cette thèse et de prêter ou de vendre des exemplaires du film.

L'auteur (titulaire du droit d'auteur) se réserve les autres droits de publication; ni la thèse ni de longs extraits de celle-ci ne doivent être imprimés ou autrement reproduits sans son autorisation écrite.

ISBN 0-315-33940-3

MEASUREMENTS OF PROTON TOTAL REACTION CROSS SECTIONS
FOR NICKEL-58, NICKEL-60, AND CALCIUM-48 BETWEEN
22 AND 48 MeV

BY

TIJEN ELIYAKUT

A thesis submitted to the Faculty of Graduate Studies of
the University of Manitoba in partial fulfillment of the requirements
of the degree of

MASTER OF SCIENCE

© 1986

Permission has been granted to the LIBRARY OF THE UNIVERSITY OF MANITOBA to lend or sell copies of this thesis, to the NATIONAL LIBRARY OF CANADA to microfilm this thesis and to lend or sell copies of the film, and UNIVERSITY MICROFILMS to publish an abstract of this thesis.

The author reserves other publication rights, and neither the thesis nor extensive extracts from it may be printed or otherwise reproduced without the author's written permission.

ABSTRACT

Using a standard beam attenuation technique, proton total reaction cross sections, σ_R , for Ni^{58} , Ni^{60} , Ca^{48} have been measured at seven incident proton energies in the laboratory energy range from 22 to 48 MeV at the University of Manitoba Cyclotron Laboratory. The results obtained have an absolute accuracy of 1 to 3% for Ni^{58} and Ni^{60} , and 2 to 5% for Ca^{48} .

The results for Ca^{48} have been compared with both relativistic and non-relativistic optical model analyses of elastic $p+\text{Ca}^{48}$ data. The Ni^{58} and Ni^{60} results were compared both with non-relativistic optical model predictions using global parameters and a relativistic optical model analysis using a standard mixture of potential terms. Nuclear transparency calculations have been made for these nuclei using all published data below 100 MeV. Using previously measured σ_R values for nuclei from Si^{28} to Zn^{68} , along with the present measurements, σ_R variations as a function of N and Z have also been studied.

ACKNOWLEDGEMENT

I would like to thank my supervisor Dr. W.T.H. van Oers for his guidance, support and constructive criticism which stimulated my interest in this work. I would also like to express my deepest gratitude to Dr. R.F. Carlson who introduced me to the methods of data analysis and experimental technique and who showed me that it is possible to derive an enormous amount of pleasure from the pursuit of research in nuclear physics. It is a great pleasure to thank Dr. E.D. Cooper for his guidance and valuable suggestions related to the relativistic data analysis and several sections of this thesis. I wish to express my thanks to Dr. J. Birchall, Dr. A.J. Cox and Dr. R.H. McCamis for their help in the data collection and for many useful discussions. Particular thanks are due to the technical staff of the University of Manitoba Cyclotron Laboratory whose help and cooperation are appreciated.

Special thanks are reserved for my fiancee, Dr. R.M. Koshko who has given me continuing encouragement, understanding and for enduring so patiently the division of my attention during the preparation of this thesis.

TABLE OF CONTENTS

ABSTRACT.....	I
ACKNOWLEDGEMENTS.....	II
I. INTRODUCTION.....	1
I.1. NON-RELATIVISTIC MODELS.....	2
I.1.a. Nuclear Transparency Calculations.....	2
I.1.b. The Optical Model with Global Parameters.....	3
I.2. THE RELATIVISTIC OPTICAL MODEL.....	5
II. EXPERIMENTAL SET-UP AND PROCEDURE.....	9
II.1. BEAMLINE.....	9
II.2. REACTION CROSS SECTION APPARATUS.....	11
II.3. ELECTRONICS.....	15
II.3.a. Logic Operations.....	15
II.3.b. Electronic Details.....	17
II.4. TARGETS.....	20
II.5. EXPERIMENTAL PROCEDURE.....	21
III. DATA ANALYSIS.....	24
III.i. DATA REDUCTION.....	24
III.1.a. Elastic Correction.....	25
III.1.b. Large Angle Charged Particle Reaction Correction.....	25

III.1.c. Small Angle Charged Particle Reaction Correction.....	26
III.1.d. Correction Due to the Reactions in Detector 6.....	26
III.1.e. Correction of False Events Due to Detector 5.....	27
III.1.f. Other Corrections.....	27
III.2. NON-RELATIVISTIC OPTICAL MODEL ANALYSIS.....	27
III.2.a. Nuclear Transparency Calculations.....	27
III.2.b. The Optical Model with Global Parameters...	28
III.3. RELATIVISTIC OPTICAL MODEL ANALYSIS.....	29
IV. RESULTS AND DISCUSSIONS.....	34
IV.1. NICKEL-58.....	34
IV.2. NICKEL-60.....	46
IV.3. CALCIUM-48.....	56
IV.4. SUMMARY.....	68
REFERENCES.....	74

I. INTRODUCTION

The total reaction cross section can be calculated from a simplified model where one considers the nucleon-nucleus interaction as a sum of nucleon-nucleon interactions, specifically, in the Glauber multiple scattering approximation at higher energies (>100 MeV), or from the optical model which assumes a uniform potential representing the nucleon-nucleus interactions.

The total reaction cross section, σ_R , provides information of fundamental importance to any full understanding of the nuclear interaction. In earlier optical model studies, [Ref. 1-4] the imaginary part of the potential did not conform to any systematic behaviour. Since then studies have indicated that the imaginary parameters are quite sensitive to the total reaction cross section. The σ_R data, to a large extent, determine the imaginary potential in the optical model [Ref. 5, 6]. Also σ_R measurements provide a great deal of information on few nucleon studies [Ref. 5]. In addition, the total reaction cross section provides an important constraint on phase shift analyses of nucleon elastic scattering.

I.1. NON-RELATIVISTIC MODELS

I.1.a. Nuclear Transparency Calculations

Many of the earlier reaction cross section studies at energies up to 100 MeV were concerned with the behaviour of σ_R as a function of mass number at a single energy [Ref. 6-14]. However, recently the energy dependence of σ_R (except at lower energies where the Coulomb barrier reduces σ_R substantially) has been established and is represented by the following semi-geometrical relation [Ref. 12, 15-17]

$$\sigma_R = \pi (r_0 A^{1/3} + \lambda)^2 \left(1 - \frac{zZe^2}{r_0 A^{1/3} E} \right) (1 - T) \quad (1)$$

where λ is the reduced wavelength for the relative motion of the incident particle and the target, r_0 is the radius parameter, ze and E are the charge and center-of-mass energy of the incident particle, Ze is the nuclear charge, and T is the energy dependent nuclear transparency which is related to the mean free path of the incident particle inside the target nucleus. In general, the cross section increases with increasing energy up to a maximum near 20 MeV, decreases to a minimum between 100 and 300 MeV, and then slightly increases with increasing energy (up to 1000 MeV) due to pion production [Ref. 15]. Hence [Eq. 1] represents a way of separating σ_R values into a geometrical factor and a factor which depends on the nuclear reaction mechanism. In this two-parameter model representation of the reaction cross section, the radius parameter, which is fixed for each nucleus, determines the geometrical cross section while the energy-dependent nuclear transparency, T , is associated with the nuclear reaction mechanism.

I.1.b. The Optical Model with Global Parameters

Over the years an extensive search for a better understanding of the nucleon-nucleus interaction has established the optical model as one of the most widely used methods of data analysis, and frequent applications of the optical model have gradually led to modifications of the model parameters to improve the fits. The conventional optical model replaces the aggregate of nucleons with a potential having several parameters contained in complex central plus complex spin-orbit terms. The optical potential used in our analysis was of the standard form

$$U(\vec{r}) = V_c(\vec{r}) - Vf(x_0) + i4a_1 W_{sf} \frac{d}{dr} f(x_1) - iW_{vo} f(x_1) + (V_{so} + iW_{so}) \frac{4}{r} \left[\frac{d}{dr} f(x_{so}) \right] \vec{S} \cdot \vec{L} \quad (2)$$

where V_c is the Coulomb potential and is represented by the potential of a uniformly charged sphere:

$$V_c(\vec{r}) = \frac{ze^2}{2r} \left[3 - \left(\frac{r}{R} \right)^2 \right], \quad r \leq R \\ = \frac{ze^2}{r}, \quad r > R \quad (3)$$

where R is the Coulomb radius, $R=r_0 A^{1/3}$ fm, with r_0 taken to be 1.25 fm, as suggested by Menet [Ref. 7]. However the r_0 values for each nucleus, taken from the charge distribution compilation suggested by Hofstadter might yield better agreement [Ref. 51]. V is the real potential, W_{vo} and W_{sf} are the volume and surface parts of the imaginary potential, respectively, and V_{so} is the real part of the spin-orbit potential. The imaginary part of the spin-orbit potential, W_{so} , was set equal to zero since its negligible value has no

significant effect on the quality of the fits, although it becomes quite an important parameter at energies of 500 MeV and higher. The radial form factor, $f(x_a)$ is a Fermi function:

$$f(x_a) = [1 + \exp(x_a)]^{-1} \quad \text{where}$$

$$x_a = \frac{r - r_a A^{1/3}}{a_a} \quad (4)$$

The optical potential thus contains six geometrical parameters, namely, $r_o, a_o, r_i, a_i, r_{so}, a_{so}$ and five dynamical parameters: $V, W_{vo}, W_{sf}, V_{so}, W_{so}$.

Based on the fact that the quality of the fits with fixed geometry and strength is comparable to the best fits to each individual target nucleus, the global parameters from Becchetti and Greenlees [Ref. 4] have been adopted here. In their work, they analyzed existing elastic scattering data for incident protons of energies up to 50 MeV scattering from nuclei of mass number between 40 and 90, and determined an optimum general parameter set using the standard formulation of the optical model. Although the superiority of the global parameters over the parameters that were extracted from the individual analyses has not been established, it has been shown that [Ref. 3, 4], within the range of validity, the global parameters can be used with reasonable confidence.

I.2. THE RELATIVISTIC OPTICAL MODEL

During the last decade an optical model based on the Dirac equation has been developed as an alternative to the Schrödinger equation based phenomenology [Ref. 18-30]. This is largely due to the availability of the experimental elastic scattering data for spin observables. The basic feature of the standard relativistic optical model is the treatment of the optical potential as a mixture of a Lorentz scalar potential and the time-like component of a four-vector potential which provides the required spin-orbit and central terms. This (SV) model was motivated by the fact that heavy mesons play an important role in the description of nuclei, and furthermore the effective nucleon-nucleus interaction is derivable from the meson-exchange models of the two-nucleon interaction. In this model the scalar potential is related to the neutral scalar field arising from a two-pion exchange process, and similarly, the vector potential is related to the neutral vector field composed of ω -mesons. However, the model assumption of a static field is not fulfilled since the struck particle recoils. Although a model of this type has been successfully applied to the finite nuclear size and the single particle bound state problems, one can also consider other combinations which use a tensor potential to obtain the large spin-orbit strength, such as (ST), (VT), or (SVT). However it has been pointed out that there is an unsolved ambiguity in their Lorentz character, but there is some theoretical evidence from the relativistic impulse approximation and relativistic nuclear structure calculations which favours the (SV) model [Ref. 29, 31]. The (SV) model has recently been applied over a wide

energy range (20-400 MeV) with encouraging results [Ref. 29, 31], including systematic behaviour in this energy range, which is a basic requirement for any type of phenomenological model.

The most general local, time independent Dirac equation contains five types of potentials: scalar, pseudoscalar, vector, axial vector and tensor. But under the applications of conservation laws, such as parity conservation and time reversal invariance, only scalar, vector and tensor potentials remain. Hence the Dirac equation has the following form:

$$\{\vec{\alpha} \cdot \vec{p} + \beta(M+S) - (E-V) + i\beta\vec{\alpha} \cdot \hat{r}T\} \psi(\vec{r}) = 0 \quad (5)$$

The vector contains the static Coulomb potential, while the tensor T contains the potential due to the interaction of the anomalous magnetic moment of the projectile with the charge distribution of the nucleus. After a series of algebraic manipulations, one obtains the second order Dirac equation in the following form:

$$\begin{aligned} & \{V^2 + (E-V)^2 - (M+S)^2 - V^r{}^2 - T^2 \\ & + \left[\frac{1}{rA} \frac{\partial A}{\partial r} - \frac{2T}{r} \right] \vec{\sigma} \cdot \vec{L} - \frac{2}{r} (iV^r + T) \\ & + \frac{1}{A} \frac{\partial A}{\partial r} (iV^r + T) + \frac{1}{r} (\vec{r} \cdot \vec{p})(V^r - iT) \\ & - \left[i \frac{1}{rA} \frac{\partial A}{\partial r} - 2 \frac{V^r}{r} \right] \vec{r} \cdot \vec{p} \} \psi_u(\vec{r}) = 0 \end{aligned} \quad (6)$$

where $A = (M + S + E - V) / (M + E)$ and V^r is the 3-vector part of the vector potential (V is the time-like component of the vector potential).

From this point one defines

$$\psi_u(\vec{r}) = K(\vec{r})\phi(\vec{r}) \quad (7)$$

with $K(r) \rightarrow 1$ as $r \rightarrow \infty$. Direct substitution of [Eq. 7] into [Eq. 6] gives

$$\frac{\partial}{\partial r} K(\vec{r}) = \frac{1}{2} \left[\frac{1}{A} \frac{\partial A}{\partial r} + 2iV^r \right] K(\vec{r}) \quad (8)$$

Using [Eq. 8], one may write the Schrödinger equivalent equation

$$\begin{aligned} & \{ \nabla^2 + (E-V)^2 - (M+S)^2 - T^2 + \frac{T}{A} \frac{\partial A}{\partial r} - 2 \frac{T}{r} \\ & - \frac{\partial T}{\partial r} - \frac{3}{4} \frac{1}{A^2} \left(\frac{\partial A}{\partial r} \right)^2 + \frac{1}{2r^2 A} \frac{\partial}{\partial r} (r^2 \frac{\partial A}{\partial r}) \\ & + \left(\frac{1}{rA} \frac{\partial A}{\partial r} - 2 \frac{T}{r} \right) \vec{\sigma} \cdot \vec{L} \} \phi(\vec{r}) = 0. \end{aligned} \quad (9)$$

It is clear that the 3-vector part of the vector potential does not appear in [Eq. 9]. From here one can define the Schrödinger equivalent central, spin-orbit and Darwin potentials, they are:

$$\begin{aligned} U_{\text{cent.}} &= \frac{1}{2E} \left\{ 2EV + 2MS - V^2 + S^2 + T^2 + 2 \frac{T}{r} - \frac{T}{A} \frac{\partial A}{\partial r} \right. \\ & \quad \left. + \frac{\partial T}{\partial r} + \frac{3}{4A^2} \left(\frac{\partial A}{\partial r} \right)^2 - \frac{1}{2r^2 A} \frac{\partial}{\partial r} (r^2 \frac{\partial A}{\partial r}) \right\}, \\ U_{\text{s.o.}} &= \frac{1}{2E} \left\{ - \frac{1}{rA} \left(\frac{\partial A}{\partial r} \right) + \frac{2}{r} T \right\} \quad \text{and,} \\ U_{\text{D}} &= \frac{1}{2E} \left\{ - \frac{1}{2r^2 A} \frac{\partial}{\partial r} (r^2 \frac{\partial A}{\partial r}) + \frac{3}{4A^2} \left(\frac{\partial A}{\partial r} \right)^2 \right\}, \end{aligned} \quad (10)$$

for a Schrödinger equation given by

$$\vec{p}^2 + 2E(U_{\text{cent.}} + U_{\text{s.o.}} \vec{\sigma} \cdot \vec{L}) \phi(\vec{r}) = (E^2 - M^2) \phi(\vec{r}) \quad (11)$$

It is clear that both the central and spin-orbit potentials depend on S , V and T , while there is no tensor contribution to the Darwin potential. Since pseudoscalar and axial vector terms can be omitted because of a parity argument, and since the tensor coupling of the ω -meson is thought

to be small, it follows that the scalar and vector potentials alone are adequate to describe our system. In order to compare the relativistic optical model at low energies with the non-relativistic model, the Dirac equation must be reduced to a Schrödinger equation for the upper components of ψ for the (SV) model in a similar manner to that above. (i.e. deletion of the tensor potential and anomalous magnetic moment term.)

II. EXPERIMENTAL SET-UP AND PROCEDURE

II.1. BEAMLINE

The experiment was carried out at the University of Manitoba Cyclotron Laboratory. The proton beam leaving the cyclotron was centered with respect to the axis of the beamline by using the combination magnet and varying the stripping foil angle. Steering magnets ST11, ST12 and the quadrupole lenses Q1 and Q2 were also used. The beam of the cyclotron was brought to a waist at the position of the slit system S1 which defined the object size for the rest of the beam transport system. The slit setting of S1 was 0.1 cm wide by 0.05 cm high. The beamline configuration is shown in [Fig. 1]. The proton beam was momentum analyzed and deflected into the 15° right beamline and into the reaction cross section apparatus by the bending magnet. A beam limiter (a circular carbon block with a 1.8 cm by 0.75 cm rectangular hole) was placed just before the bending magnet. During the experiment, the quadrupole lens Q3 was turned off, while Q4 was used to retract the focal plane of the bending magnet onto the location of the image slits (with an aperture of dimensions 0.3 cm high by 0.2 cm wide).

By using a small current source the residual magnetic field (39 Gauss) of the analyzing magnet "A" was nulled to avoid the deflection of protons to the high resolution beamline. A set of collimators, described in the following section, were used to further define the beam size and direction.

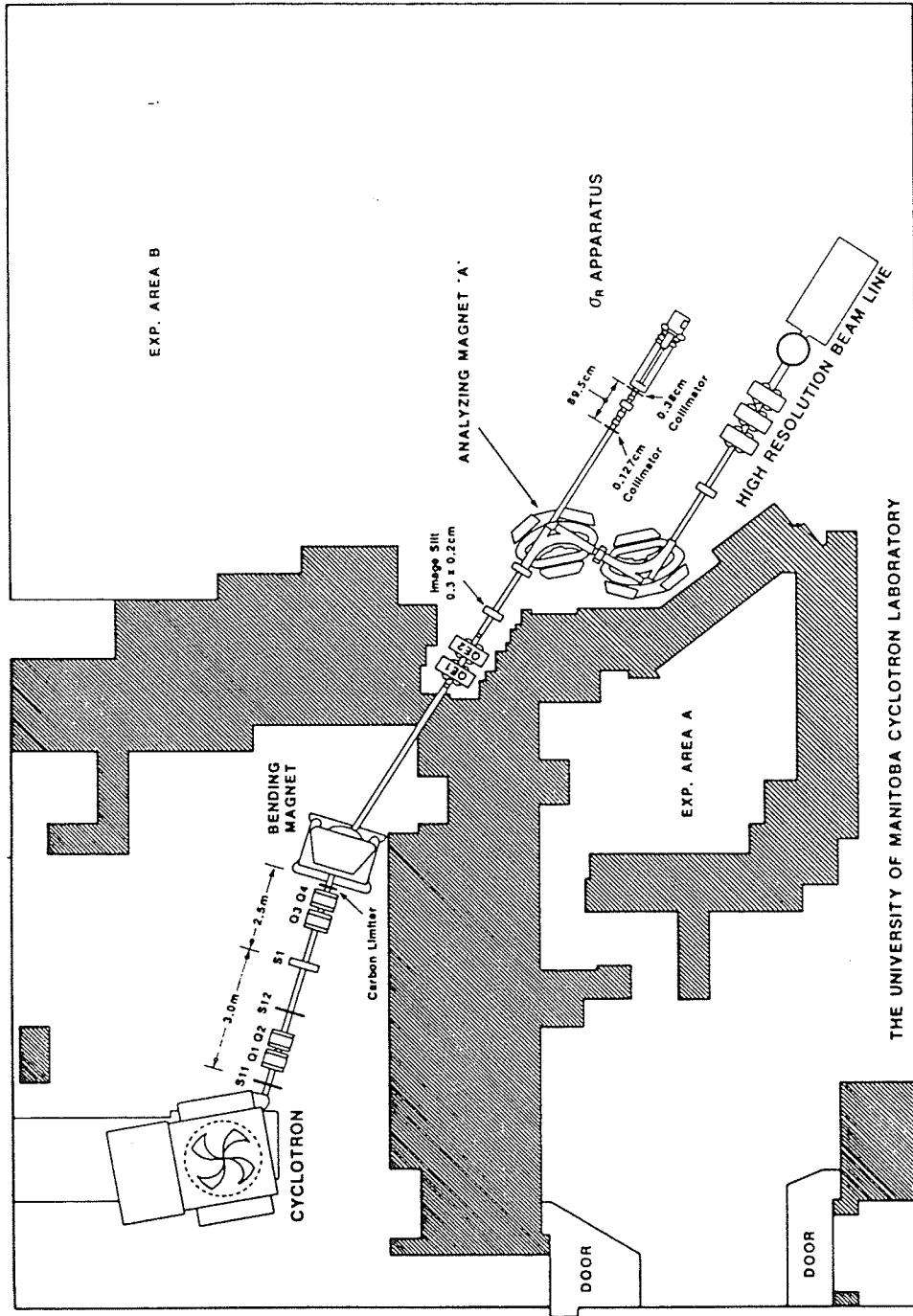


[Fig. 1]
Beam Line Configuration

11.2. REACTION CROSS SECTION APPARATUS

The reaction cross section apparatus consists of an evacuated tube fitted with a circular entrance collimator of 0.127 cm diameter [Fig. 2]. A brass antiscattering baffle, with a 0.38 cm diameter hole is located 89.5 cm away from the first collimator. The antiscattering baffle removes the protons scattered from the edge of the circular collimator.

The passing detectors 1 and 2 are two plastic scintillators constructed from NE-102 sheet and are .0064 cm and .0076 cm thick, respectively. They were separated by a distance of 6.0 cm. Each of the scintillators is mounted in a cylindrical tube, the inner surface of which is coated with white reflecting paint. One end of the tube is closed while the other end is open for viewing by a photomultiplier tube through a lucite window which also forms a vacuum seal. The beam enters and leaves the cylindrical tube through 1.3 cm diameter holes in the sides which are covered with 0.0006 cm thick aluminized mylar, thus optically isolating each tube from the other. Passing detector 1 is located 10.9 cm downstream from the antiscattering baffle while passing detector 2 is separated by 0.3 cm from the first scintillator disc of annular detector 3.

The annular detector telescope is composed of detectors 3 and 4. Detector 3 consists of a pair of plastic scintillator discs. The first disc has a hole 0.236 cm in diameter, while the second disc has a hole 0.305 cm in diameter. Each scintillator is mounted in a lucite holder

which is covered with aluminized mylar; the assembly slides into a cavity in the apparatus. The discs are held perpendicular to the beam. The distance between the two discs of annular detector 3 is 2.5 cm, and the second disc is 19.2 cm from the target location. Each cavity is vacuum sealed with a lucite disc, and both ends are viewed by photomultiplier tubes. Annular detector 4 is a scintillator disc with a center hole of 0.368 cm diameter and is located 4.9 cm upstream from the target position.

The target foils are mounted on a target wheel 10.3 cm in diameter. The wheel can accommodate 14 targets plus an empty space for target-out measurements. The wheel is turned by an electric motor which is fitted with a synchro-readout, allowing the target to be positioned remotely from the control room. Immediately following the target is a collimator which defines the acceptance angle subtended by the energy analyzing detector system. This angle was 45° for the three targets used in this experiment.

The energy analyzing system consists of two detectors. The first of these, detector 5, is a small plastic scintillator disc of 0.635 cm diameter and 0.102 cm thickness placed in a flat lucite pipe 0.157 cm thick which passes out through slots in the target block for viewing by two photomultiplier tubes. Each photomultiplier tube views one end of the light pipe through a lucite window. Detector 5 subtends a cone of half-angle 8° with respect to the center of the target. Protons which emerge from a target with deflection between 0° and 8° will strike detector 5. The electronic logic treats such protons as non-reactions,

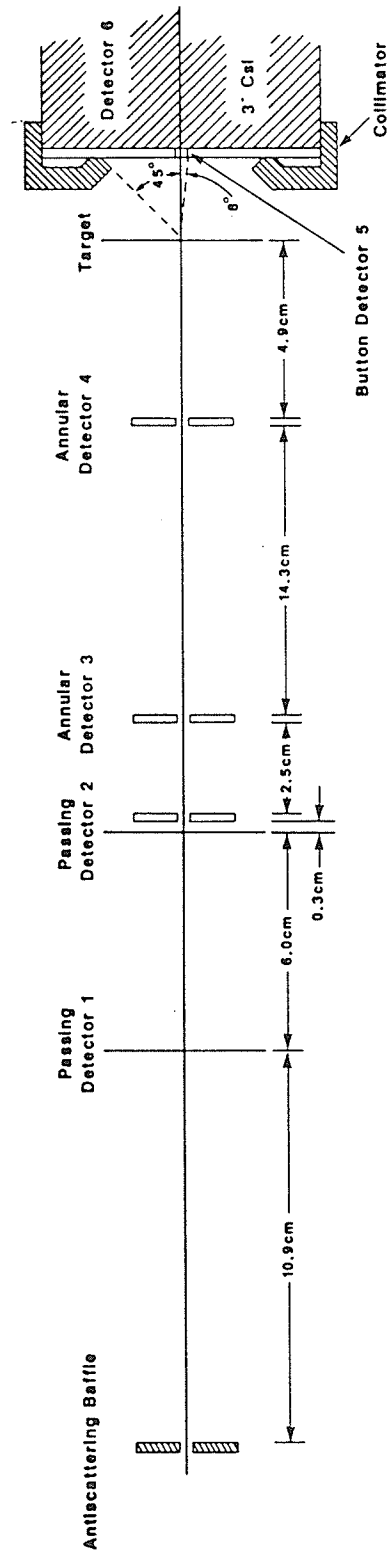


[Fig. 2]
Schematic diagram of the total reaction cross section apparatus.

whether they deposit full energy in the stopping detector 6 or not. In general, 98% or more of the beam particles passing through the targets emerge in the 8° cone, almost all having been elastically or multiple Coulomb scattered. These protons produce 98% or more of the reactions in the stopping detector 6, causing false reactions to be recorded. A very small number of protons have undergone reactions in the target, and a small error is made because these reaction products are treated as non-reactions. As a result of the presence of detector 5, the attenuation rate $(i_0 - i)/i_0$ with target-out is reduced by a large factor; it no longer contributes significantly to the overall statistical error. The stopping detector 6 is a Cesium Iodide crystal 8.9 cm in diameter and 1.3 cm thick coupled to a photomultiplier tube through a lucite light pipe. Detector 6 is located directly behind detector 5.

II.3. ELECTRONICS

II.3.a. Logic Operations

The electronic circuitry can be briefly divided into three major parts (see [Fig. 3]). The first part selects a proton with the correct characteristics from the incident beam by imposing a double coincidence anticoincidence requirement on the signals generated in detectors 1, 2, 3 and 4. The pulse resulting from this selection circuit is recorded as an I_0 pulse. Once an I_0 event occurs, the second part of the electronic circuitry is activated. The function of this section is to determine whether or not the incident proton has been removed by the target. If it is not, this circuit generally produces an I pulse. I and I_0 are combined in the third logic circuit to form $(I_0 - I)$, which represents the number of protons removed from the beam by the target. It can be measured directly and is related to the total reaction cross section.

An I_0 pulse is produced whenever pulses are generated in passing detectors 1 and 2 in coincidence in the absence of pulses from both annular detectors 3 and 4. This event is denoted $1\bar{2}\bar{3}\bar{4}$ and indicates that a proton has passed unscattered through the passing detectors 1 and 2 and has passed through the central portion of the annular detectors 3 and 4. This I_0 pulse is routed into two branches. One branch opens the normally closed linear gate while the other branch goes to the signal input of a normally open linear gate (after being delayed). If the proton which produced the $1\bar{2}\bar{3}\bar{4}$ pulse does not undergo a reaction and is elastically scattered from 0° to the maximum acceptance angle of

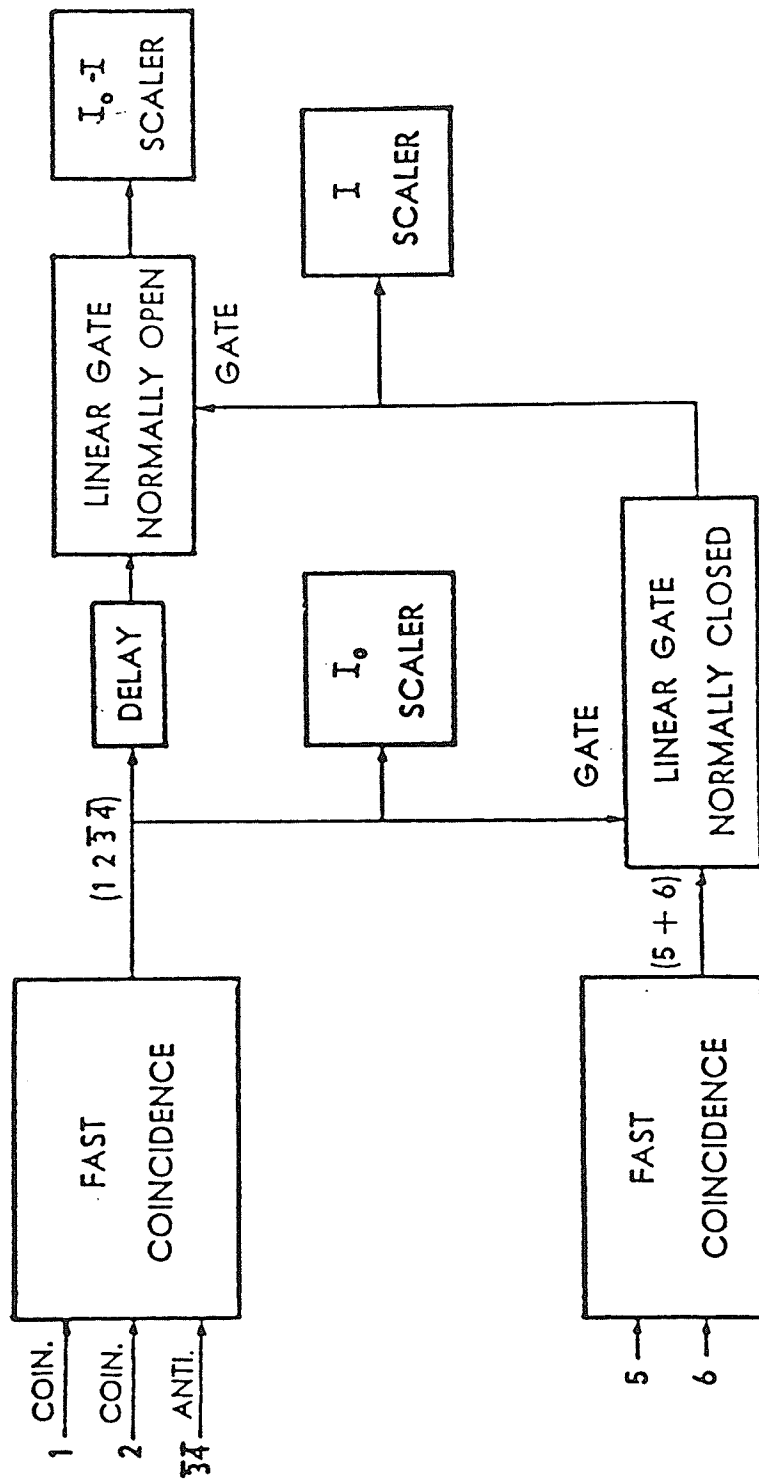


[Fig. 3]
Block diagram of the electronic logic operation.

detector 6, a second pulse is generated and is denoted by (5+6). This (5+6) pulse passes through the linear gate opened by the $12\overline{34}$ pulse, registers as an I event, and closes the normally open linear gate, preventing the delayed $12\overline{34}$ pulse from passing through the linear gate and registering as an ($I_0 - I$) event. However, if the proton undergoes a reaction in the target, it does not, in general, produce a (5+6) pulse. The normally open linear gate remains open and the delayed $12\overline{34}$ pulse passes through and registers as an ($I_0 - I$) event.

II.3.b. The Electronic Details

Fast signals from the anodes of passing detectors 1 and 2 were amplified in the experimental area and transmitted to the electronic setup in the control room. These pulses were fed through fast discriminators. An additional discriminator was used for detector 2 to obtain a short pulse for the pile-up gate. The negative outputs from the discriminator chains for detectors 1 and 2 were fed into a 4-fold logic unit (coincidence-1), which operated in the two-fold coincidence mode. The summed signal from the anodes of the photomultipliers viewing detector 3 was amplified in the experimental area and the same was done for detector 4. After passing through the fast discriminators, these signals were fed into a fan-in unit. The output from the fan-in unit was connected to the lo-veto input of the pile-up gate which produces an inhibit pulse wherever a pulse was received from the fan-in unit. The pile-up gate was also connected to inhibit input of the coincidence-1. Therefore, the output from the coincidence-1 was $12\overline{34}$, (i.e. the I_0

pulse).

The linear signals from the dynodes of detectors 5 and 6 were preamplified and amplified in the experimental area, then fed into the single channel analyzers used as integral discriminators. Negative signals from these integral discriminators were fed into a fan-in unit. The output of this unit was $(5+6)$ (i.e. an I pulse). The logic pulses $12\bar{3}4$ and $(5+6)$ now drive linear gates in the manner described in section II.3.a.

Positive signals from the integral discriminators for detectors 5 and 6 were delayed and sent to the coincidence-2 unit. This unit produced an output when the I_0 signal was in coincidence with the signal from the detector 6 and in anticoincidence with the signal from detector 5. The output of this coincidence unit was sent to the $E\bar{B}$ scalar. The unipolar output pulse from the detector 6 linear amplifier was delayed and routed to the signal input of a normally closed linear gate which was opened by the presence of the output signal from the coincidence-2 unit. The output of the linear gate was fed into an analog-to-digital converter (ADC) which was interfaced to a VAX/VMS version V4.3 computer, the gated spectrum of detector 6 being stored in a 1024 channel memory. The purpose of this circuitry was to help in determining certain corrections discussed in Chapter III.

Accurate reaction cross section measurements require precise timing of the circuit elements, especially the gates. In particular, the normally closed gate opened by an I_0 pulse must remain open long enough

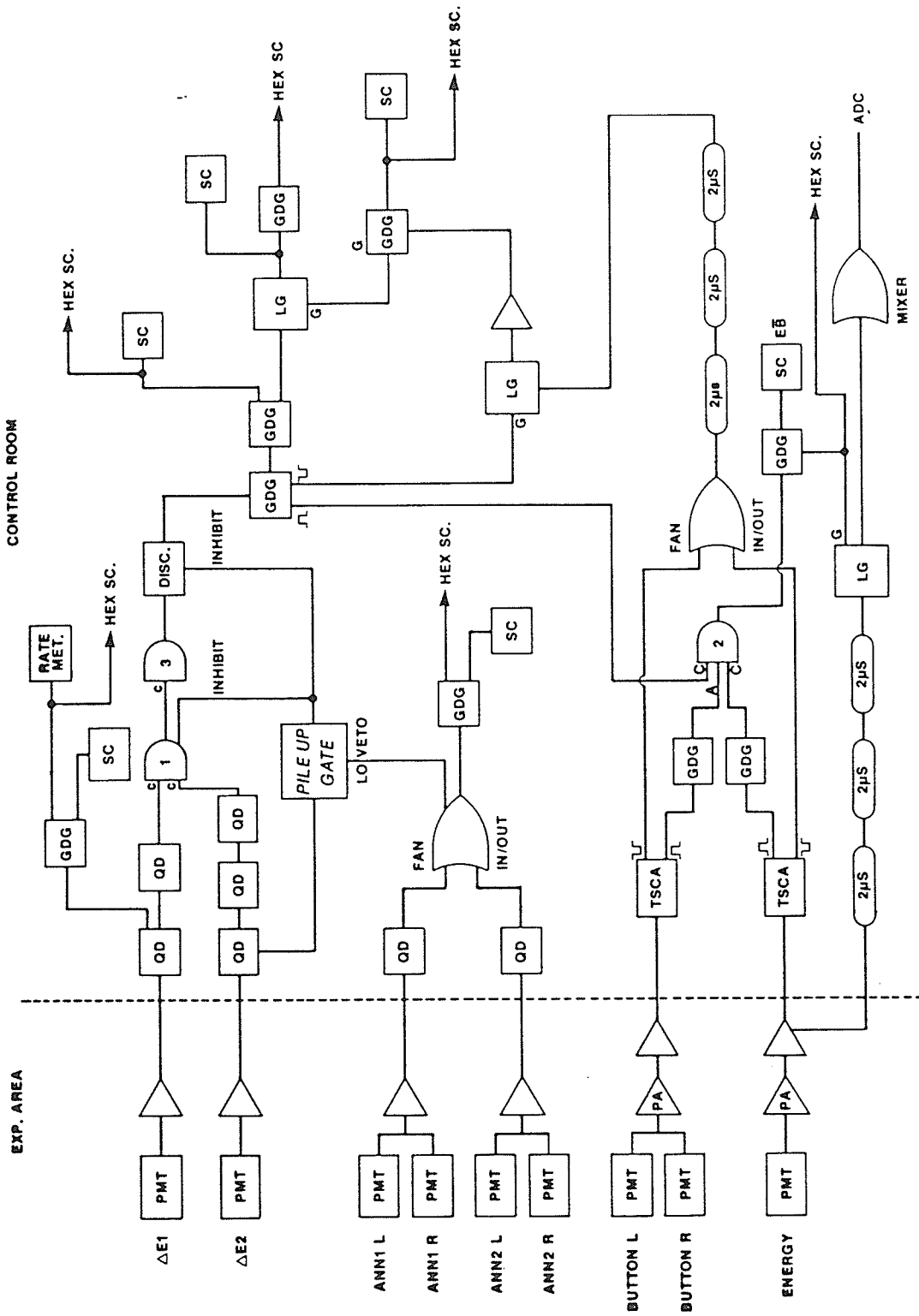


[Fig. 4]
Block diagram of the electronic circuit.

for the associated I pulse, if any, to pass through. The normally open gate, when closed by the I pulse, must remain shut long enough to block the I_0 pulse completely. To eliminate errors caused by pile-up effects, an artificial dead time was introduced into the electronic system by means of a pile-up gate. This unit produces an inhibit pulse whenever it receives a pair of input pulses from detector 2 spaced less than t seconds apart. The pile-up resolving time t was selected to be 6 μ sec. (The inhibit pulse remained as long as pairs were received within 6 μ sec; whenever two pulses were spaced less than 6 μ sec apart, the pile-up reject circuitry rejected both pulses, and hence no I_0 pulse was produced.) An appropriate delay, 6 μ sec, was introduced on the coincidence-3 signal [Fig. 4].

II.4. TARGETS

Circular targets of Ni^{58} and Ni^{60} , 1.26 cm in diameter, were used for the σ_R measurements of nickel. These stable nickel targets were 99.79% enriched for Ni^{58} and 99.07% for Ni^{60} . For calcium measurements a 90.81% enriched Ca^{48} target 1.26 cm in diameter was used. The Ca^{48} target was handled with extra care to avoid oxygen contamination. For the Ca^{48} target instalment, the target block, which contains its own pumping system, was removed from the σ_R apparatus and transferred into a glove box filled with 99.9995% purified argon gas. (The sum of N_2 , O_2 , CO_2 , H_2O , etc. was less than 5 ppm.) Immediately after weighing the target, it was mounted on the target wheel. Then the target block was removed from the glove box while the

whole block was flushed with argon gas and transferred back to the σ_R apparatus. After completion of the experiment, the Ca^{48} target was weighed again in the glove box to determine any possible oxygen contamination. An electronic balance was used to determine the mass to an accuracy of ± 0.1 mg. The Ni^{58} and Ni^{60} targets were also weighed before and after the experiment. The areal density of each target was determined from the ratio of its mass to its area. The overall accuracies in determining the areal densities varied between 0.4% and 2.4%. The areal densities of the targets are given in [Table 1].

II.5. EXPERIMENTAL PROCEDURE

The experiment consisted of a series of target-in and target-out measurements at each energy. A threshold was set on detector 6, 6 MeV below the elastic peak. The master scalar was set to stop counting the incident protons I_0 when $10^7 I_0$ events had been recorded. The beam intensity was monitored so that the incident beam rate did not exceed 10^4 protons per second. At each energy at least three runs of $10^7 I_0$ events were taken for each target.

During the experiment, the incident proton energy was varied seven times in the energy range from 23 to 48 MeV. The energy of the beam was changed by altering the magnetic field of the bending magnet. A nuclear magnetic resonance (NMR) probe was used to measure the magnetic field. The calibration was determined by the use of a modified range-energy technique suggested by Bichsel [Ref. 49, 50]. The beam was reduced in energy by an accurately lapped silicon degrader. The residual beam

[Table 1]

Areal Densities of the Targets

Target	$\rho x \pm \Delta\rho x$ (mg/cm ²)	$n x \pm \Delta n x$ (nuclei/cm ²) $\times 10^{20}$
Ni ⁵⁸	40.53 \pm 0.21	4.21 \pm 0.02
Ni ⁶⁰	39.48 \pm 0.14	3.97 \pm 0.01
Ca ⁴⁸	10.44 \pm 0.25	1.31 \pm 0.03

energy was then measured by a Si surface-barrier detector. The 5.47 MeV alpha line from Am^{241} was used along with a precision pulser to calibrate the silicon detector. The thickness of silicon required to stop this residual beam was determined from the range-energy tables for silicon of Bichsel [Ref. 49, 50] and this was added to the thickness of the degrader, giving the total amount of silicon required to stop the full energy of the incident beam. The range-energy tables were used again to determine the incident proton energy. Three energy points in the range 23 to 48 MeV were measured to calibrate the bending magnet. A table of energy versus NMR frequency was generated. By this method, the beam energy was determined to within 100 KeV. The beam energy spread after collimation was about ± 150 KeV.

III. DATA ANALYSIS

III.1 DATA REDUCTION

The attenuation of a beam of particles passing through matter is given by

$$I = I_0 \exp(-nx\sigma) \quad (12)$$

where I_0 and I are the intensities of the incident beam and attenuated beam, respectively, n is the number of nuclei per unit volume in the target, x is the target thickness, and σ is the attenuation cross section. If $(nx\sigma)$ is small compared to unity, [Eq. 12] can be re-written as,

$$\sigma = \frac{(I_0 - I)}{nxI_0} \quad (13)$$

From this point, the uncorrected reaction cross section was obtained from the following formula:

$$\sigma_{un} = \frac{1}{nx} \left[\frac{(I_0 - I)}{I_0} - \frac{(i_0 - i)}{i_0} \right] \quad (14)$$

where $(I_0 - I)$ and $(i_0 - i)$ are the number of attenuation events with target-in and target-out, respectively. I_0 and i_0 the number of incident protons with target-in and target-out, respectively, and nx is the number of target nuclei per cm^2 . The total reaction cross section was obtained by applying a series of corrections to the uncorrected reaction cross section σ_{un} [Ref. 32-34].

III.1.a. Elastic Correction

A proton elastically scattered from the target at an angle greater than the maximum acceptance angle subtended by the detector 5 and 6 telescope (45°) is not a reaction. Yet it is treated like one by the logic. Thus the experimentally measured cross section must be corrected by subtracting the elastic differential cross section integrated from 45° to 180° . To compute this correction, all available elastic scattering data for each target in the energy range under study were collected from the literature [Ref. 3,8,31,35-41]. The angular distributions were integrated numerically and the results plotted as a function of energy. Points at the energies of the experiment were obtained by a second-order polynomial fit to the integrated results.

III.1.b. Large Angle Charged Particle Reaction Correction

The charged particles produced by nuclear reactions which are scattered into detector 6 between angles 8° and 45° (hence, missing detector 5) with energies above its discriminator level, which was set 6 MeV below the elastic peak, will be counted as non-attenuation, I, events. A correction must be applied to the measured cross section for these missing events. This correction was obtained in a similar manner to that for the elastic correction. All available inelastic differential cross section data for excited state energies up to 6 MeV for the targets under study was collected from the literature [Ref. 31,35-36,41-44] and integrated over the 8° - 45° angular range. An interpolation was then made and the corresponding correction was added to the measured cross

section.

III.1.c. Small Angle Charged Particle Reaction Correction

All charged particles entering detector 5 within the 0° - 8° angular range and depositing energy above the noise level in the detector (about 0.4 MeV) will produce an I pulse (non-attenuation event). These reaction events are also missed, and a correction must be added to the uncorrected reaction cross section. Since the solid angle subtended by detector 5 at the target is small, 0.077 sr, this correction is quite small in general and it may be calculated in a way similar to the large angle correction.

III.1.d. Correction Due To The Reactions In Detector 6

Protons which are elastically scattered into detector 6 while missing detector 5 may initiate nuclear reactions with the detector 6 CsI scintillator, producing false ($I_0 - I$) events. This correction must be subtracted from the uncorrected reaction cross section. This correction was obtained by using the appropriate known reaction probability for a proton stopping in CsI [Ref. 45]. The number of protons entering detector 6 and missing detector 5 is counted during the experiment and the associated cross section is multiplied by the reaction probability.

III.1.e. Correction Of False Events Due To Detector 5

Detector 5 is a scintillator disc embedded in a flat lucite light pipe. A proton elastically scattered from the target and subsequently scattered in the lucite in such a way that it does not enter detector 6 gives a false attenuation event. A correction must be subtracted from the measured total reaction cross section. In general this correction has been found to be 2 mb or less [Ref. 32-34]. In the present experiment this correction ranged from 1 to 2 mb.

III.1.f. Other Corrections

Two other possible corrections, namely due to finite beam size and finite target thickness were found to be negligible [Ref. 32-34] compared to the overall experimental error. Thus they were neglected in the final result.

Particles scattered from the target or reaction products between the angles 173° and 180° impinge on the second annular detector and this give a condition of an invalid incident beam particle. This effect has been evaluated and mainly due to the small solid angle present a negligible correction.

III.2. NON-RELATIVISTIC OPTICAL MODEL ANALYSIS

III.2.a. Nuclear Transparency Calculations

The following procedure which is similar to that of De Vries and Peng [Ref. 16] was applied to our experimental reaction cross section results along with all the published data for the nuclei of this experiment below 100 MeV [Ref. 45]. First, the radius parameter r_0 was determined for each nucleus by solving [Eq. 1] for r_0 after setting $T=0$ and using all experimental values of σ_R for that nucleus. The largest r_0 value was arbitrarily taken to be the fixed value for r_0 for that particular nucleus. Next, using the fixed r_0 value and keeping $T=0$ in [Eq. 1], geometrical σ_R values were calculated at each experimental energy. These reaction cross section values correspond to a totally absorbing or black nucleus and are called $\sigma_R(bl)$. Finally, [Eq. 1] was solved for T , using experimental σ_R values and previously determined r_0 values. All these results will be presented in Chapter IV for each nucleus under study.

III.2.b. The Optical Model Analysis with Global Parameters

Becchetti and Greenlees' optimum proton-nucleus standard optical model parameters, so called global parameters, in further parameterized form in terms of A, Z, N, and E are as follows [Ref. 4]:

$$\begin{aligned}
 V &= 54 - 0.32E + 0.4 \left(\frac{Z}{A^{1/3}} \right) + 24 \left(\frac{N-Z}{A} \right) \text{ MeV} , \\
 W_{vo} &= 0.22E - 2.7 \text{ MeV, (or zero, whichever is greater) ,} \\
 W_{sf} &= 11.8 - 0.25E + 12 \left(\frac{N-Z}{A} \right) \text{ MeV, (or zero, whichever is greater),} \\
 a_I &= 0.51 + 0.7 \left(\frac{N-Z}{A} \right) \text{ fm} , \qquad (15)
 \end{aligned}$$

where E is the incident proton energy and $V_{so}=6.2$ MeV, $r_o=1.17$ fm, $a_o=0.75$ fm, $r_i=1.32$ fm, $r_{so}=1.01$ fm, and $a_{so}=0.75$ fm. The dynamical parameters, namely the real potential V, the imaginary surface and volume potentials W_{sf} and W_{vo} respectively, and the imaginary diffusivity a_i were calculated for each target nucleus for the energy range under study. By using a modified version of the program SEEK, these parameters were applied to the standard Schrödinger based phenomenology. Reaction cross sections were calculated. These results will be presented in Chapter IV.

III.3. RELATIVISTIC OPTICAL MODEL ANALYSIS

Nuclear optical model studies using the Dirac equation containing large cancelling Lorentz scalar and Lorentz four-vector potentials, have shown its superiority to the standard Schrödinger equation based phenomenology. In this work, nickel isotopes (Ni^{58} , Ni^{60}) were

studied at lower energies than previously considered [Ref. 19-31].

In the application of Dirac phenomenology to the analysis of p-Ni⁵⁸, p-Ni⁶⁰ elastic scattering, the complex potentials have been used in the following (SV) model form:

$$S = V_s f_s(\vec{r}) + iW_s g_s(\vec{r})$$

$$V = V_v f_v(\vec{r}) + iW_v g_v(\vec{r}) . \quad (16)$$

where the form-factors are two-parameter Fermi functions $[1 + \exp((r-r_i)/a_i)]^{-1}$, with $i=v, s$. The model consists of twelve adjustable parameters, the same as in the standard non-relativistic Schrödinger phenomenology. These twelve parameters were varied, using the chisquare (χ^2) minimization method, to obtain the best fit to Ni⁵⁸ and Ni⁶⁰ differential cross section and analyzing power data found in the literature [Ref. 3, 8, 35-41, 46]. The analysis began with a fit to the data at 65 MeV. This was accomplished by allowing the individual potential strengths V_v , W_v , V_s and W_s , as well as the geometrical parameters, to vary until the best fit was achieved. (The model parameters were varied one at a time until χ^2 was minimized for each individual parameter search.) The solid lines in [Fig. 5.a] and [Fig. 5.b] show the fit obtained for Ni⁵⁸ and Ni⁶⁰ at 65 MeV. The 65 MeV potential parameters were then used as the starting point for analysis at the other energies. Reasonable fits to the data at each energy were obtained by changing the strengths of the potentials and varying the shape factors as little as possible from that obtained at 65 MeV. Then, by using the potential parameters that were obtained from the

fits for each energy, the reaction cross section predictions were completed for Ni⁵⁸ and Ni⁶⁰.

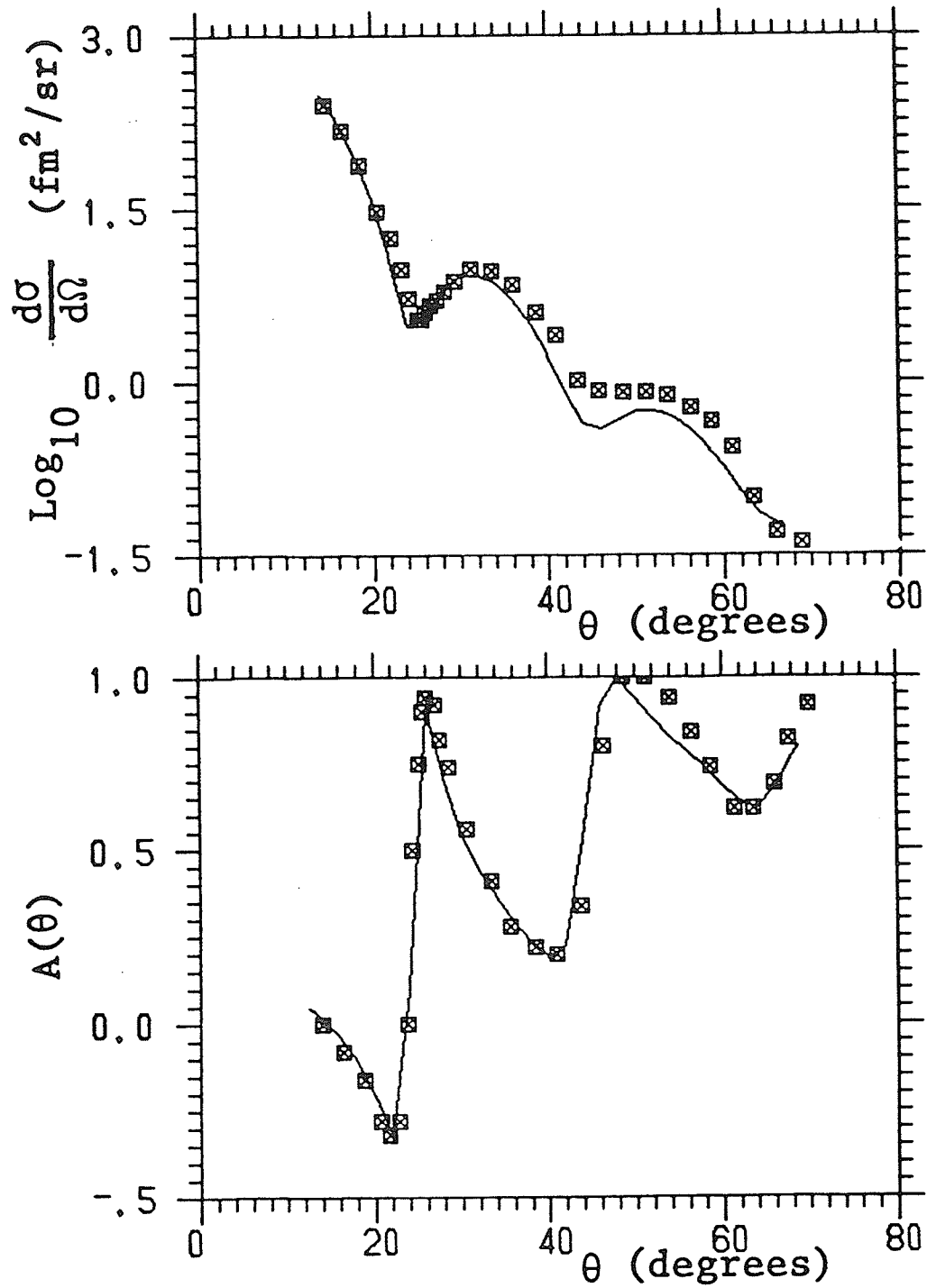


[Fig. 5.a]
 Best fit differential cross sections and analyzing powers
 for $p+\text{Ni}^{58}$ at 65 MeV using the relativistic optical model.

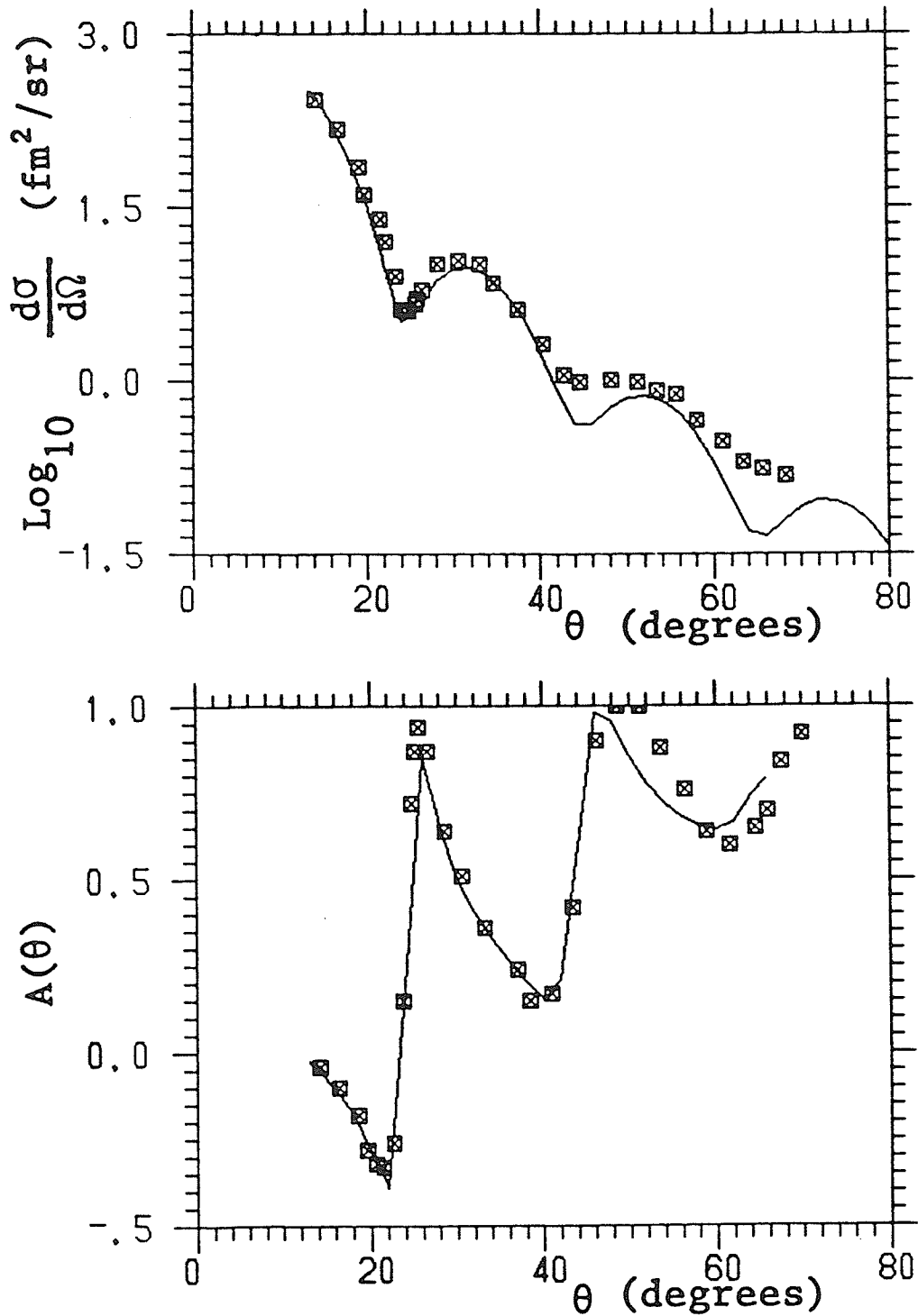


[Fig. 5.b]

Best fit differential cross sections and analyzing powers for $p+\text{Ni}^{60}$ at 65 MeV using the relativistic optical model.

IV. RESULTS AND DISCUSSIONS

IV.1. NICKEL-58

The final $p+Ni^{58}$ total reaction cross section values are shown in the last column of [Table 2], along with the associated uncertainties. The table also contains the uncorrected reaction cross section as well as the different correction terms. The main contribution to the correction of the uncorrected reaction cross section was from the elastic correction, which was about 15% of σ_{un} at the lower energies and decreased with increasing energy. The total reaction cross section values are plotted as a function of incoming proton energy for Ni^{58} in [Fig. 6]. The σ_R values vary smoothly with energy and decrease with increasing energy. A comparison of the experimental proton total cross section for Ni^{58} has been made with the other experimental values available from the literature [Ref. 7, 8] at 60, 49, 40, 30 and 28 MeV. Although, in general, reaction cross section results from the present work average about 2% higher than those from the literature, within the limits of the experimental uncertainties there exists reasonable agreement.

The results of the nuclear transparency calculations are presented in [Table 3]. The values corresponding to a black nucleus are listed under $\sigma_R(bl)$ in [Table 3] and plotted in [Fig. 7] along with the $\sigma_R(Exp)$ results. The increasing difference between $\sigma_R(Exp)$ and $\sigma_R(bl)$ values with increasing energy is attributed to an increase (from zero) of the nuclear transparency T which is listed in the last column of

[Table 2]

Proton Total Reaction Cross Sections for Ni⁵⁸

Energy (MeV)	σ_{un} (fm ²)	Elastic correct. (fm ²)	Large angle charged part. correction (8°-45°) (fm ²)	Small angle charged part. correction (0°-8°) (fm ²)	Correction for react. in the stopping detector (fm ²)	Correction for react. in detector 5 (fm ²)	σ_R (fm ²)
22.7	123.5±2.5	13.6±1.4	2.9±0.6	0.9±0.5	3.8±0.1	0.2±0.1	109.8±2.9
25.1	121.3±2.9	12.5±1.3	3.1±0.6	0.9±0.5	3.8±0.1	0.1±0.1	108.8±3.3
30.1	116.5±2.6	10.3±1.0	3.2±0.6	1.1±0.5	3.6±0.3	0.1±0.1	106.7±2.9
34.9	110.8±3.3	8.5±0.8	3.1±0.6	1.1±0.6	3.8±0.6	0.1±0.1	102.7±3.5
39.8	105.3±0.9	6.7±0.7	2.9±0.6	1.2±0.6	3.5±0.1	0.1±0.1	99.1±1.4
45.1	100.7±0.6	5.1±0.5	2.6±0.5	1.1±0.5	3.3±0.6	0.1±0.1	95.9±1.3
47.9	99.1±3.0	4.4±0.4	2.4±0.5	1.1±0.6	3.4±0.7	0.1±0.1	94.7±3.2

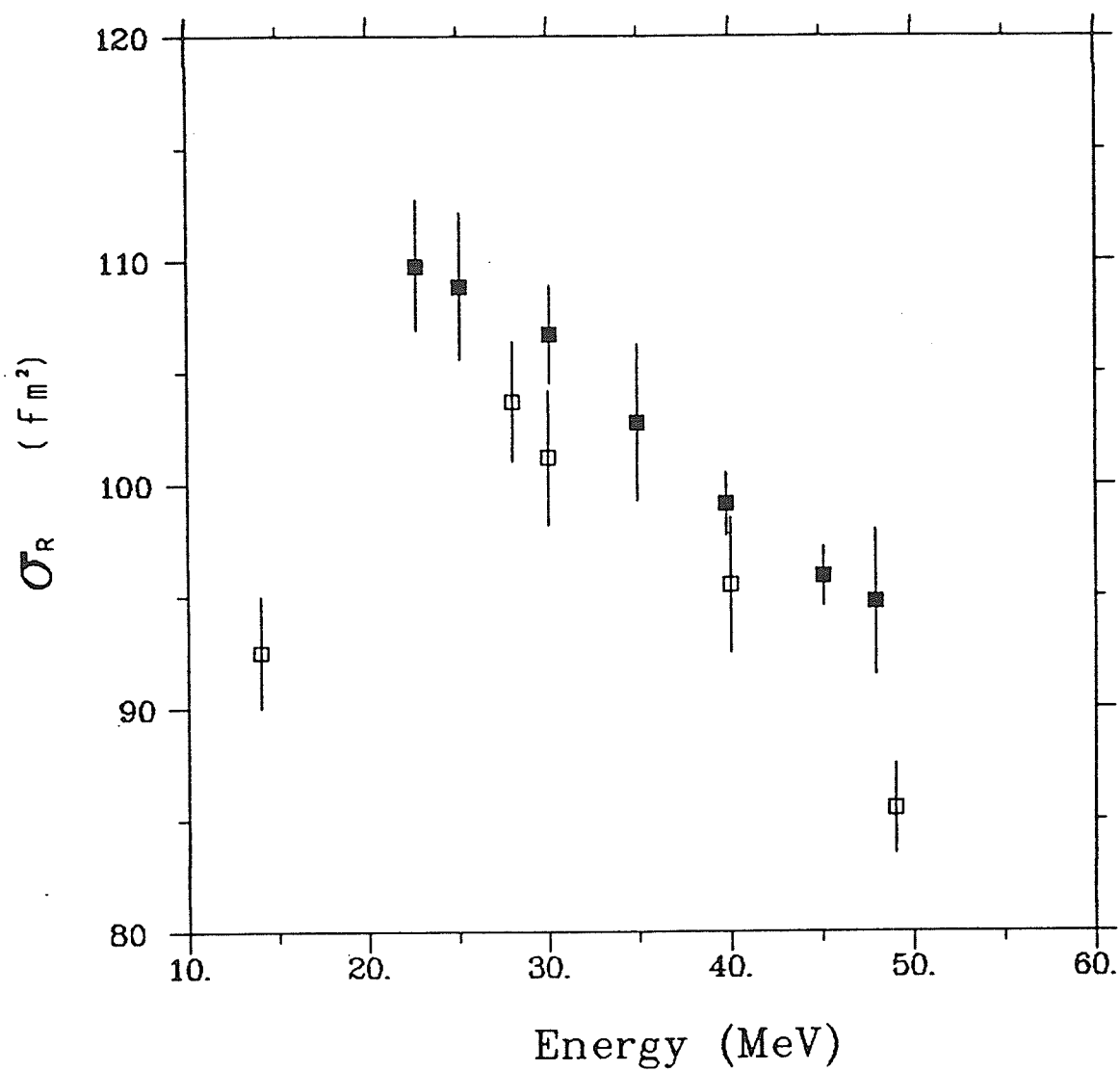


[Fig. 6]

p+Ni⁵⁸ total reaction cross sections:

■, present work; □, other lab's results.

[Table 3]

Nuclear Transparency Calculations for Ni⁵⁸

r_0 (fm)	Energy (MeV)	σ_R (Exp) (fm ²)	σ_R (b ℓ) (fm ²)	T (%)
1.53	60.8	80.7±2.5	119	32
	47.9	94.7±3.2	118	20
	49.5	85.6±2.9	119	28
	45.1	95.9±1.3	118	19
	40.1	95.5±3.4	117	19
	39.8	99.1±1.4	117	16
	34.9	102.7±3.5	116	12
	30.1	106.7±2.2	115	7
	30.0	101.1±3.0	114	12
	28.50	103.8±3.2	114	9
	25.1	108.8±2.9	112	3
	22.7	109.8±2.9	110	0
	14.5	92.7±2.7	96	4
	9.1	54.7±3.3	69	21

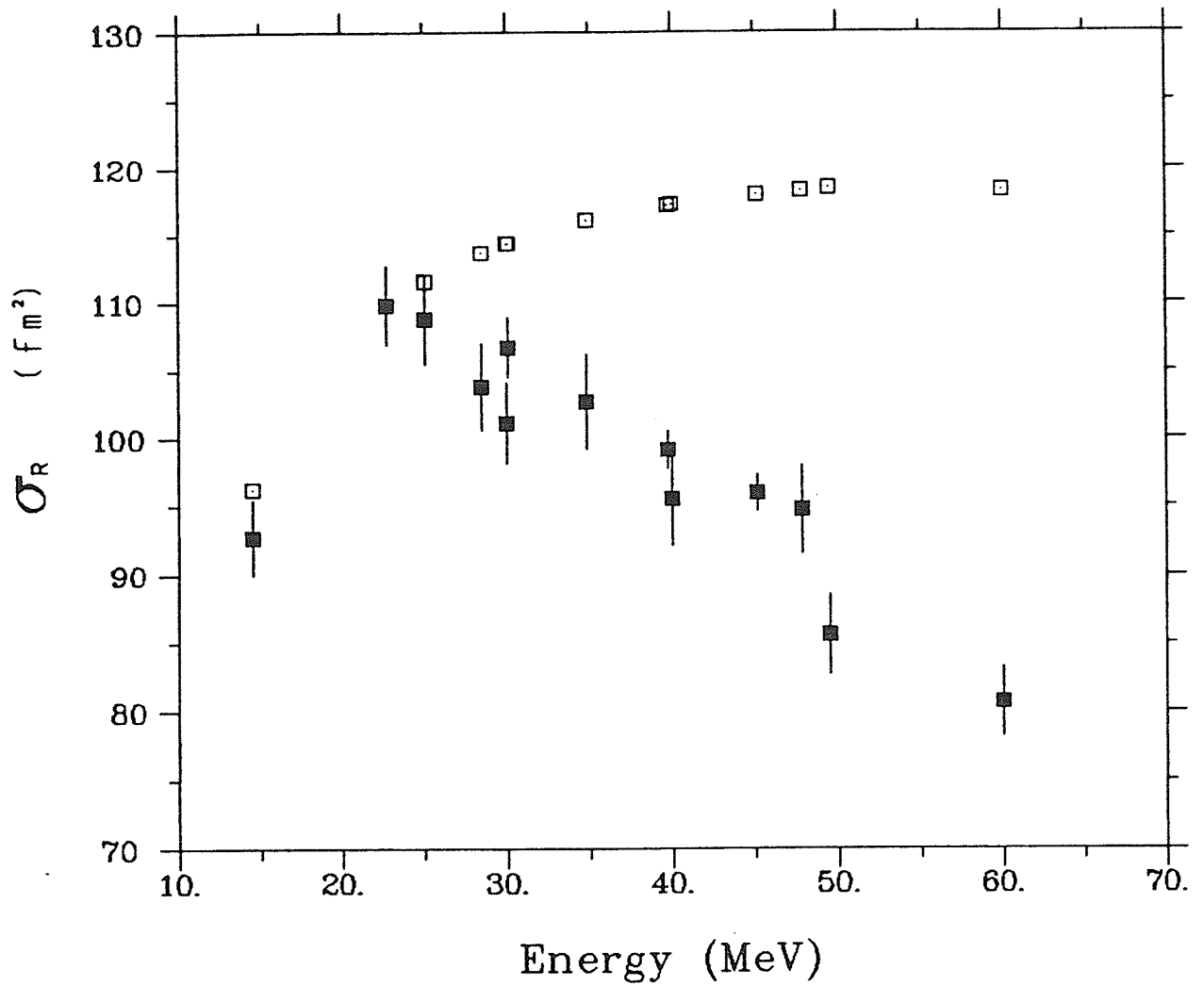


[Fig. 7]

The results of the nuclear transparency calculations
for $p+\text{Ni}^{58}$: \blacksquare , $\sigma_R(\text{Exp})$; \square , $\sigma_R(\text{bl})$.

[Table 3]. The maximum transparency, on the order of 32%, occurs for the highest incident proton energy, 60.8 MeV, while minimum transparency is obtained at 22.7 MeV. The transparency depends on the choice of radius parameter r_0 . A different r_0 value would yield a different set of transparency values. According to this model, with this choice of r_0 , Ni^{58} is almost completely absorbing around 20 or 25 MeV, and then becomes increasingly transparent to incoming protons at energies above 25 MeV.

The results of the Schrödinger equation based optical model calculations with global parameters for p- Ni^{58} elastic data are shown in [Table 4]. The theoretical total cross section, $\sigma_R(\text{theo})$, values are listed in the table together with the global parameters. The experimental total reaction cross section, $\sigma_R(\text{Exp})$, and $\sigma_R(\text{theo})$ values are plotted as a function of incident proton energy in [Fig. 8]. Although there is reasonably good agreement between experimental and theoretical reaction cross section values at energies lower than 45 MeV, within the limits of the error bars, it was observed that the $\sigma_R(\text{Exp})$ results were 4% and 7% higher than optical model reaction cross section predictions at 45 and 48 MeV, respectively.

A comparison of the experimental proton total reaction cross section for Ni^{58} has been made with the theoretical values obtained in the Dirac equation based relativistic model analysis. The potential parameters of the model are listed in [Table 5] along with the reaction cross section predictions for Ni^{58} . Although the real scalar and vector potential strengths decrease slightly with increasing energy,

[Table 4]
 Non-Relativistic Optical Model Parameters for $p+Ni^{30}$

Energy (MeV)	V (MeV)	a_o (fm)	r_o (fm)	W_{sf} (MeV)	a_i (fm)	r_i (fm)	W_{vo} (MeV)	V_{so} (MeV)	a_{so} (fm)	r_{so} (fm)	$g^2 \sigma_R$ (Theo) (fm ²)	σ_R (Exp) (fm ²)
22.73	50.44	0.75	1.17	6.52	0.53	1.32	2.30	6.20	0.75	1.01	111.5	109.8±2.9
25.08	49.68	0.75	1.17	5.93	0.53	1.32	2.82	6.20	0.75	1.01	111.2	108.8±3.3
30.10	48.08	0.75	1.17	4.67	0.53	1.32	3.92	6.20	0.75	1.01	108.6	106.7±2.9
34.84	46.56	0.75	1.17	3.49	0.53	1.32	4.96	6.20	0.75	1.01	104.1	102.7±3.5
39.77	44.98	0.75	1.17	2.26	0.53	1.32	6.05	6.20	0.75	1.01	98.6	99.1±1.4
45.13	43.27	0.75	1.17	0.92	0.53	1.32	7.23	6.20	0.75	1.01	91.6	95.9±1.3
47.85	42.40	0.75	1.17	0.24	0.53	1.32	7.83	6.20	0.75	1.01	87.8	94.7±3.2

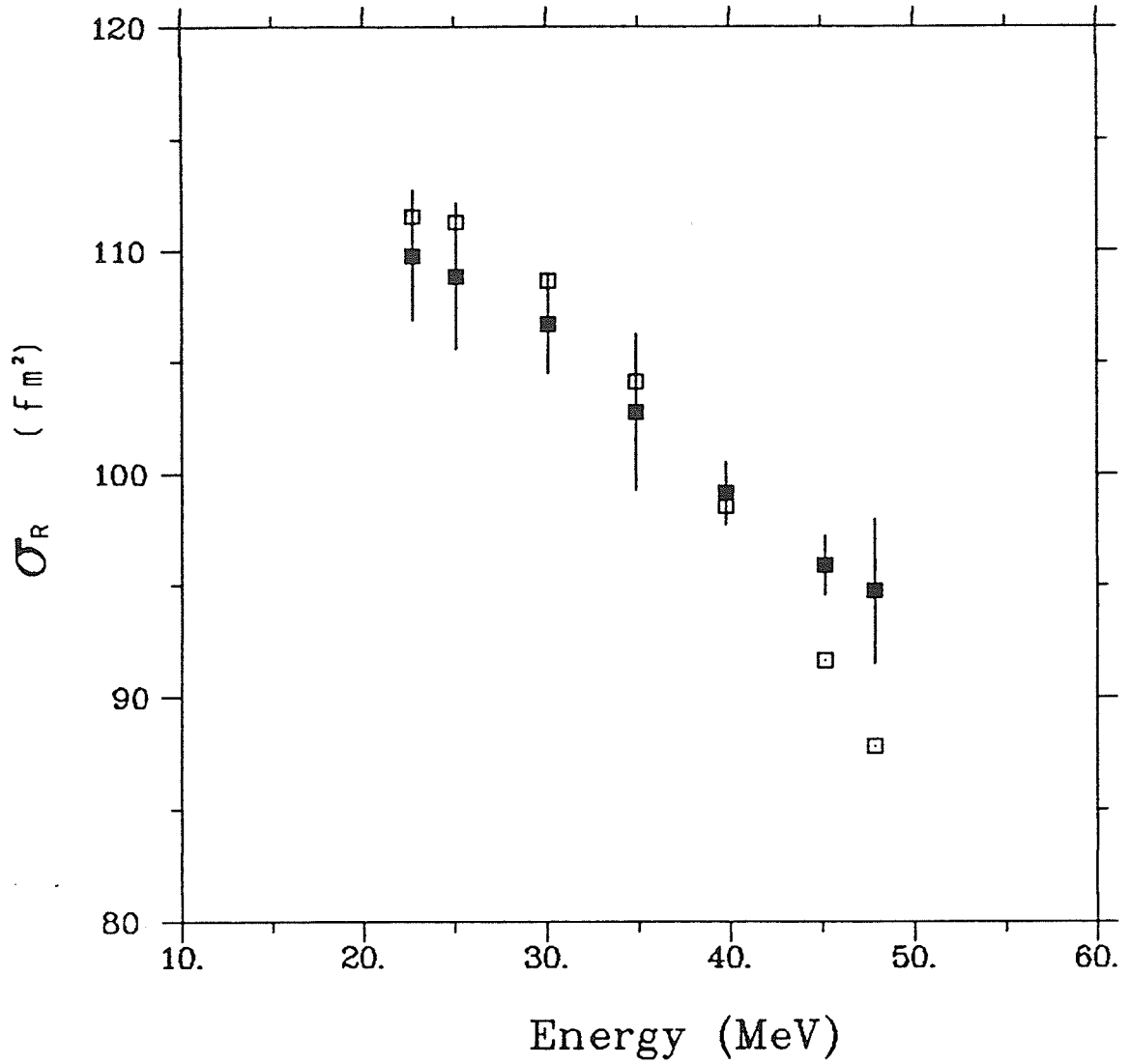


[Fig. 8]

Total reaction cross sections for $p+Ni^{58}$ using the non-relativistic optical model with global parameters: \blacksquare , $\sigma_R(\text{Exp})$; \square , $^{gl}\sigma_R(\text{Theo})$.

while the imaginary potential strengths and shape factors remain approximately the same, a strong systematic dependence of the potential parameters on varying energy is not observed. After each parameter search, χ^2 values were obtained and listed in [Table 5]. With these sets of parameters, reasonable fits to the differential cross section data were obtained at small scattering angles. The discrepancy between calculated and experimental differential cross sections at large angles (larger than 95°) is largely due to the lack of spin observables in this low energy range and for this particular nucleus; in other studies, this discrepancy was explained as a characteristic of the optical model calculations which do not include explicit exchange interactions [Ref. 28]. In further studies, inclusion of a complex l -dependent Majorana exchange potential in the optical model removed most of this large angle discrepancy [Ref. 47, 48]. A sample fit obtained from relativistic optical model analysis at 35 MeV is presented in [Fig. 9]. The total reaction cross section predictions are plotted as a function of proton energy along with the experimental reaction cross section values in [Fig. 10]. Although there is remarkable agreement between them, one must consider that it is possible another set of parameters may provide equally good agreement. The relativistic approach provides a testing ground for various relativistic structure calculations; however, at low energies, the unambiguous specification of the parameter set, and hence, the verification of the predictions, is limited by the lack of spin data.

[Table 5]

Relativistic Optical Model Parameters for $p+Ni^{58}$

Energy (MeV)	V_v (MeV)	R_v^1 (fm)	A_v^1 (fm)	W_v (MeV)	R_v^2 (fm)	A_v^2 (fm)	V_s (MeV)	R_s^1 (fm)	A_s^1 (fm)	W_s (MeV)	R_s^2 (fm)	A_s^2 (fm)	χ^2	$\sigma_R(\text{Theo})$ (fm ²)	$\sigma_R(\text{Exp})$ (fm ²)
21.3	223.0	1.038	0.645	-9.52	1.420	0.412	-277.0	1.079	0.691	4.18	1.025	0.411	12.0	111.1	
30.0	223.3	1.042	0.645	-9.52	1.420	0.412	-276.6	1.074	0.690	4.18	1.025	0.411	32.8	106.4	106.7±2.9
35.2	233.3	1.041	0.645	-9.51	1.419	0.412	-276.6	1.075	0.690	4.18	1.025	0.412	42.9	103.5	102.7±3.5
40.0	221.4	1.041	0.650	-9.52	1.430	0.411	-278.9	1.068	0.684	4.18	1.020	0.412	19.4	100.3	99.1±1.4
61.4	262.6	1.211	0.618	-7.43	1.275	0.557	-326.6	1.209	0.631	4.41	1.110	0.438	8.2	82.8	
65.0	263.7	1.214	0.615	-7.51	1.269	0.552	-324.5	1.209	0.637	4.39	1.080	0.438	178.0	81.6	

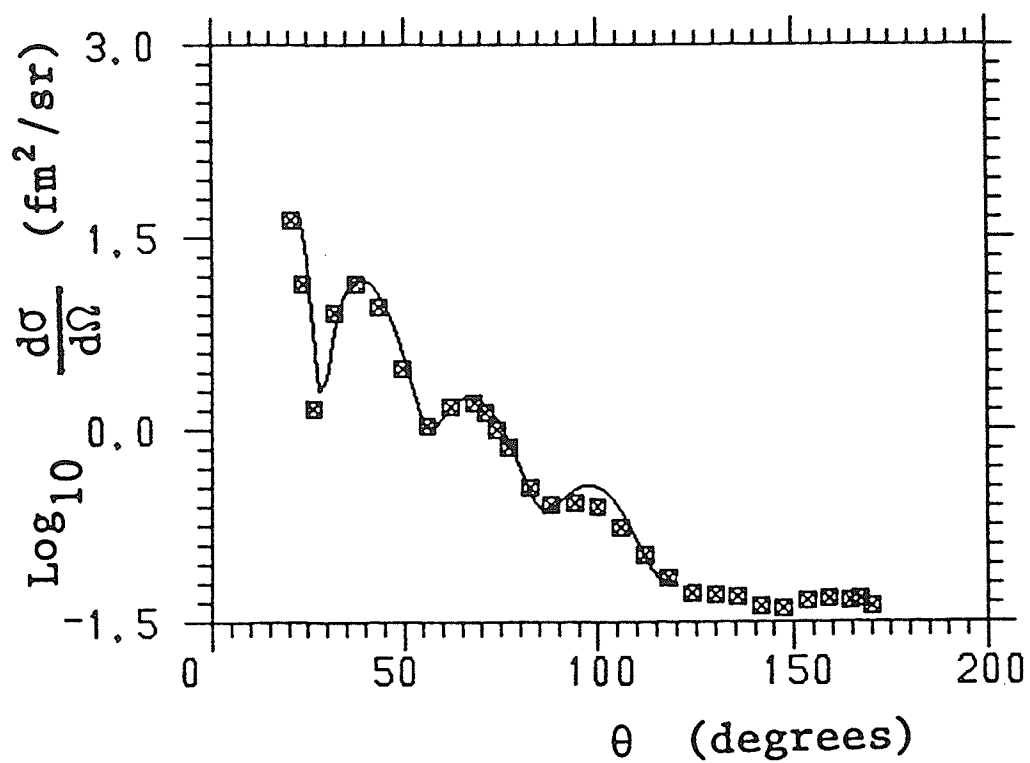


[Fig. 9]

Best fit differential cross sections for $p+\text{Ni}^{58}$
at 35 MeV using the relativistic optical model.

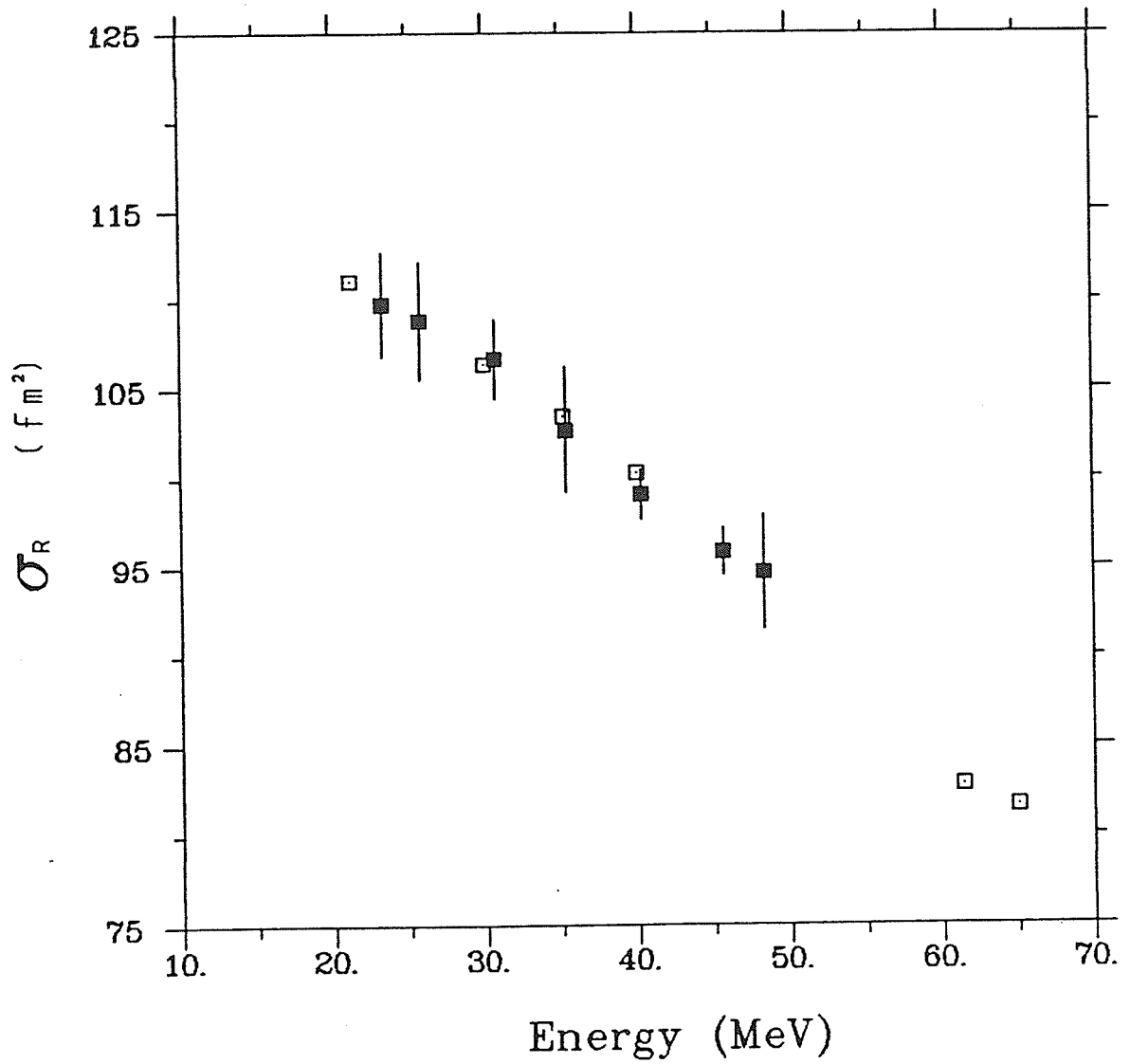


[Fig. 10]

Total reaction cross sections for $p+\text{Ni}^{58}$ using the relativistic optical model: ■, $\sigma_R(\text{Exp})$; □, $\sigma_R(\text{Theo})$.

IV.2. NICKEL-60

The measured total reaction cross section and associated corrections are presented in [Table 6]. The variation with proton energy of the proton total reaction cross section for Ni^{60} is shown in [Fig. 11], and again a smooth variation with energy was observed. A comparison of the $p+\text{Ni}^{60}$ total reaction cross section has been made with the other experimental results obtained from the literature [Ref. 6-8] at 14, 28, 40, 68 MeV. There exists considerable agreement within the limits of the uncertainties.

The results of the nuclear transparency calculations are listed in [Table 7], and $\sigma_R(\text{bl})$ and $\sigma_R(\text{Exp})$ values are plotted as a function of incoming proton energy in [Fig. 12]. The maximum transparency, on the order of 33%, occurs at 60.8 MeV, while minimum transparency is obtained at 22.75 MeV. According to this model with $r_0=1.55$ fm, Ni^{60} is almost completely absorbing around 20 to 25 MeV, and then becomes increasingly transparent to incoming protons at energies higher than 25 MeV.

The results of the non-relativistic optical model analysis with global parameters for Ni^{60} are shown in [Table 8]. The total reaction cross section of Ni^{60} is also plotted in [Fig. 13] along with the predictions derived from the non-relativistic optical model with global parameters. Reasonably good agreement was observed except at energies higher than 45 MeV. In addition, it was observed that the experimental reaction cross section at 30 MeV was 7% lower than the predicted value.

[Table 6]

Proton Total Reaction Cross Sections for Ni⁶⁰

Energy (MeV)	σ_{un} (fm ²)	Elastic correct. (fm ²)	Large angle charged part. correction (8°-45°) (fm ²)	Small angle charged part. correction (0°-8°) (fm ²)	Correction for react. in the stopping detector	Correction for react. in detector 5	σ_R (fm ²)
22.8	127.9±2.1	11.5±1.2	2.5±0.5	0.9±0.4	3.9±0.1	0.2±0.1	115.8±2.5
25.1	125.7±2.4	10.8±1.1	2.8±0.6	0.9±0.5	3.9±0.1	0.1±0.1	114.7±2.7
30.1	119.1±1.7	9.3±0.9	3.1±0.6	1.1±0.5	3.6±0.1	0.1±0.1	110.3±2.2
34.9	116.6±3.5	7.9±0.8	3.3±0.7	1.2±0.6	3.8±0.3	0.1±0.1	109.3±3.7
39.8	111.4±3.1	6.7±0.7	3.4±0.7	1.3±0.6	3.7±0.1	0.1±0.1	105.7±3.3
45.2	105.6±0.8	5.4±0.5	3.3±0.7	1.3±0.7	4.0±0.7	0.1±0.1	100.8±1.5
47.9	104.4±2.9	4.8±0.4	3.2±0.6	1.4±0.7	2.7±0.9	0.1±0.1	101.4±3.3

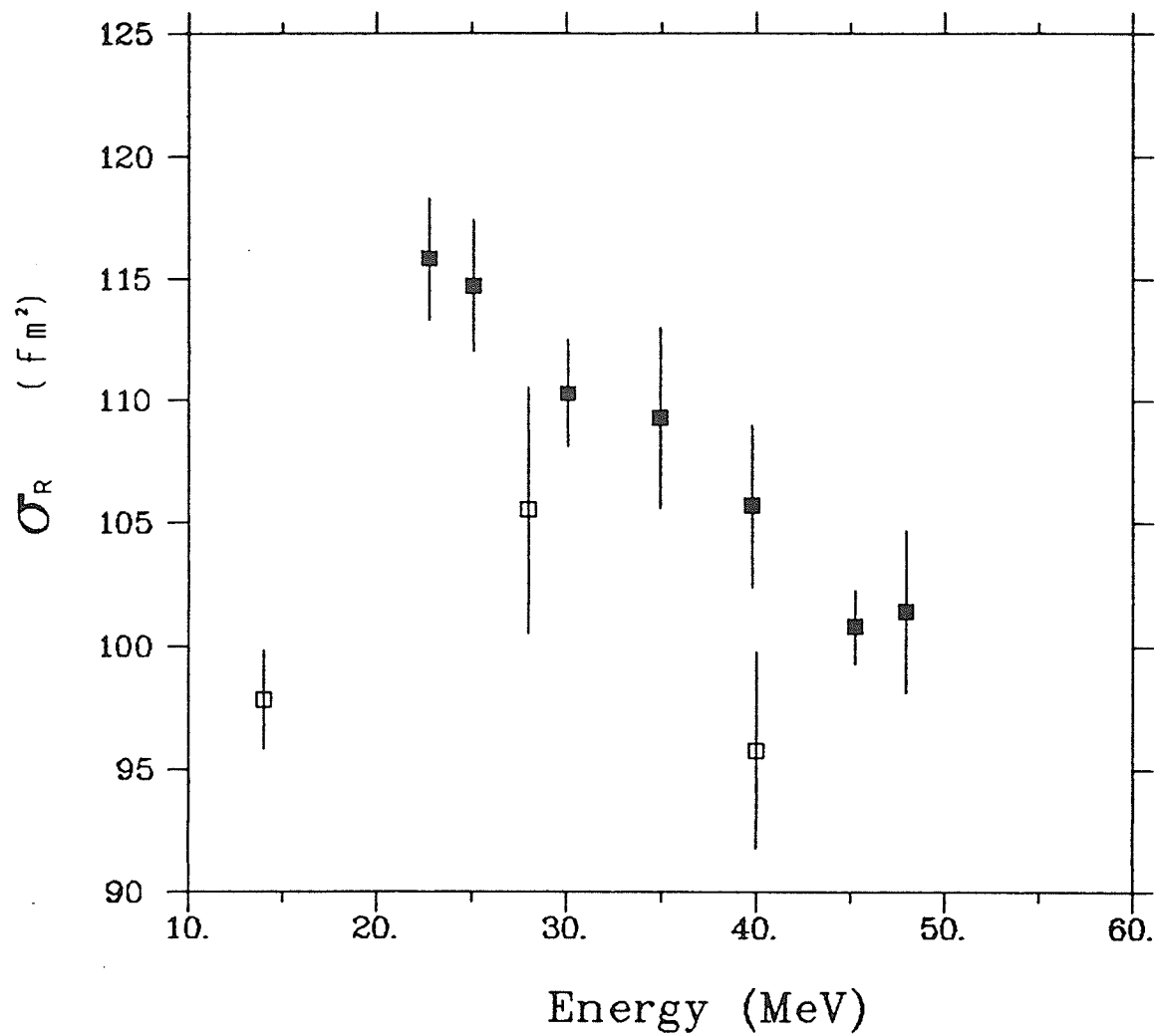


[Fig. 11]

p+Ni⁶⁰ total reaction cross sections:

■, present work; □, other lab's results.

[Table 7]

Nuclear Transparency Calculations for Ni⁶⁰

r_0 (fm)	Energy (MeV)	$\sigma_R(\text{Exp})$ (fm ²)	$\sigma_R(\text{b}\ell)$ (fm ²)	T (%)
1.55	60.8	84.1±3.0	125	33
	47.9	101.4±3.3	125	19
	45.2	100.8±1.5	125	19
	40.0	98.2±4.2	123	20
	39.8	105.7±3.3	123	14
	34.9	109.3±3.7	122	11
	30.1	110.3±2.2	121	9
	28.5	105.3±5.1	120	12
	25.1	114.7±2.7	118	3
	22.8	115.8±2.5	116	0
	14.5	97.8±1.6	102	4
	9.2	70.9±3.7	75	6

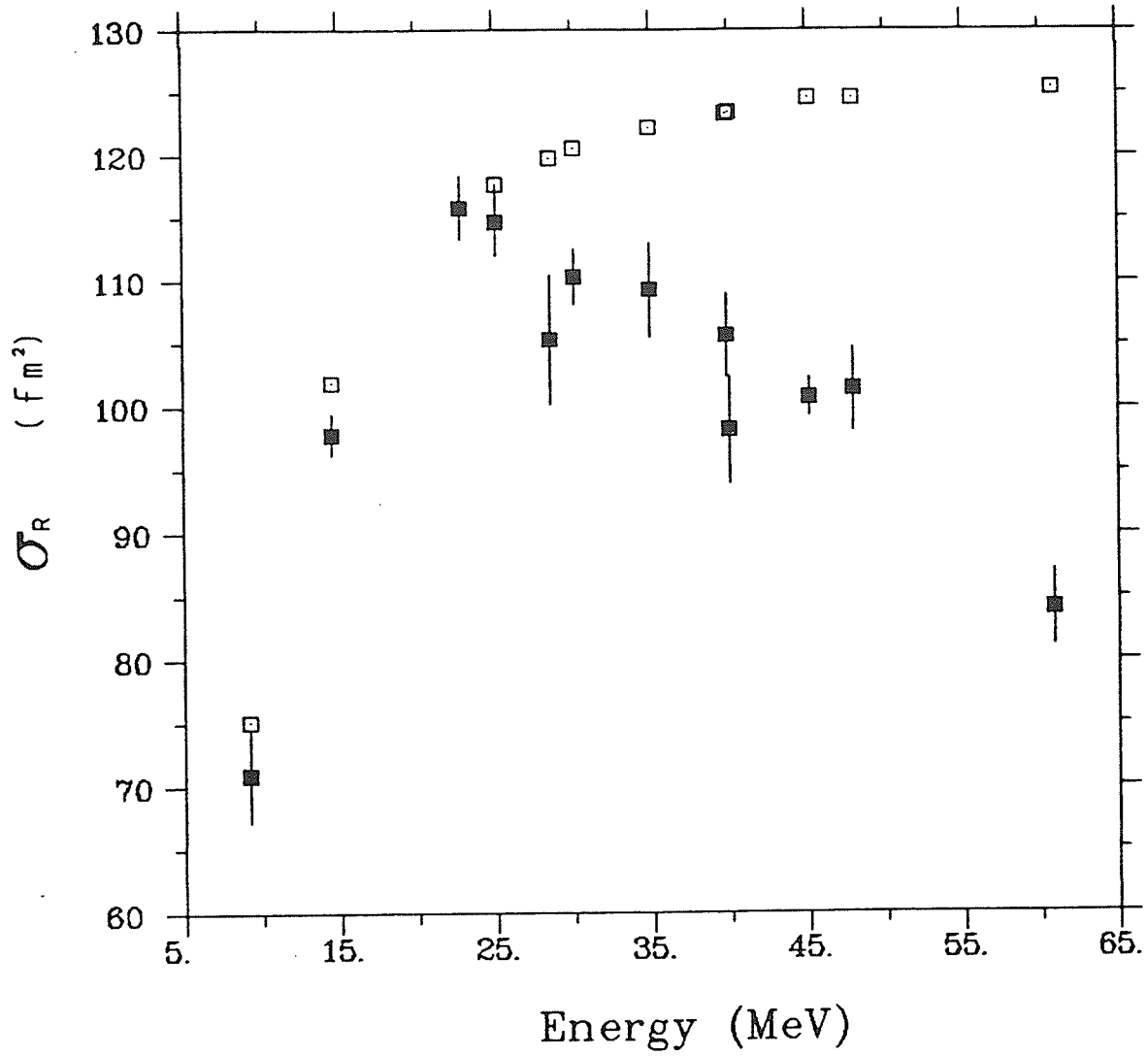


[Fig. 12]

The results of the nuclear transparency calculations
for $p+\text{Ni}^{60}$: ■, $\sigma_R(\text{Exp})$; □, $\sigma_R(\text{bl})$.

[Table 8]

Non-Relativistic Optical Model Parameters for $p+^{60}\text{Ni}$

Energy (MeV)	V (MeV)	a_o (fm)	r_o (fm)	W_{sf} (MeV)	a_i (fm)	r_i (fm)	W_{vo} (MeV)	V_{so} (MeV)	a_{so} (fm)	r_{so} (fm)	$g^2 \sigma_R(\text{Theo})$ (fm ²)	$\sigma_R(\text{Exp})$ (fm ²)
22.75	51.18	0.75	1.17	6.91	0.57	1.32	2.31	6.20	0.75	1.01	117.2	115.8±2.5
25.09	50.43	0.75	1.17	6.33	0.57	1.32	2.82	6.20	0.75	1.01	117.2	114.7±2.7
30.12	48.82	0.75	1.17	5.07	0.57	1.32	3.93	6.20	0.75	1.01	114.7	110.3±2.2
34.86	47.31	0.75	1.17	3.89	0.57	1.32	4.97	6.20	0.75	1.01	110.4	109.3±3.7
39.79	45.73	0.75	1.17	2.65	0.57	1.32	6.05	6.20	0.75	1.01	104.9	105.7±3.3
45.15	44.01	0.75	1.17	1.31	0.57	1.32	7.23	6.20	0.75	1.01	97.9	100.8±1.5
47.86	43.14	0.75	1.17	0.64	0.57	1.32	7.83	6.20	0.75	1.01	94.1	101.4±3.3

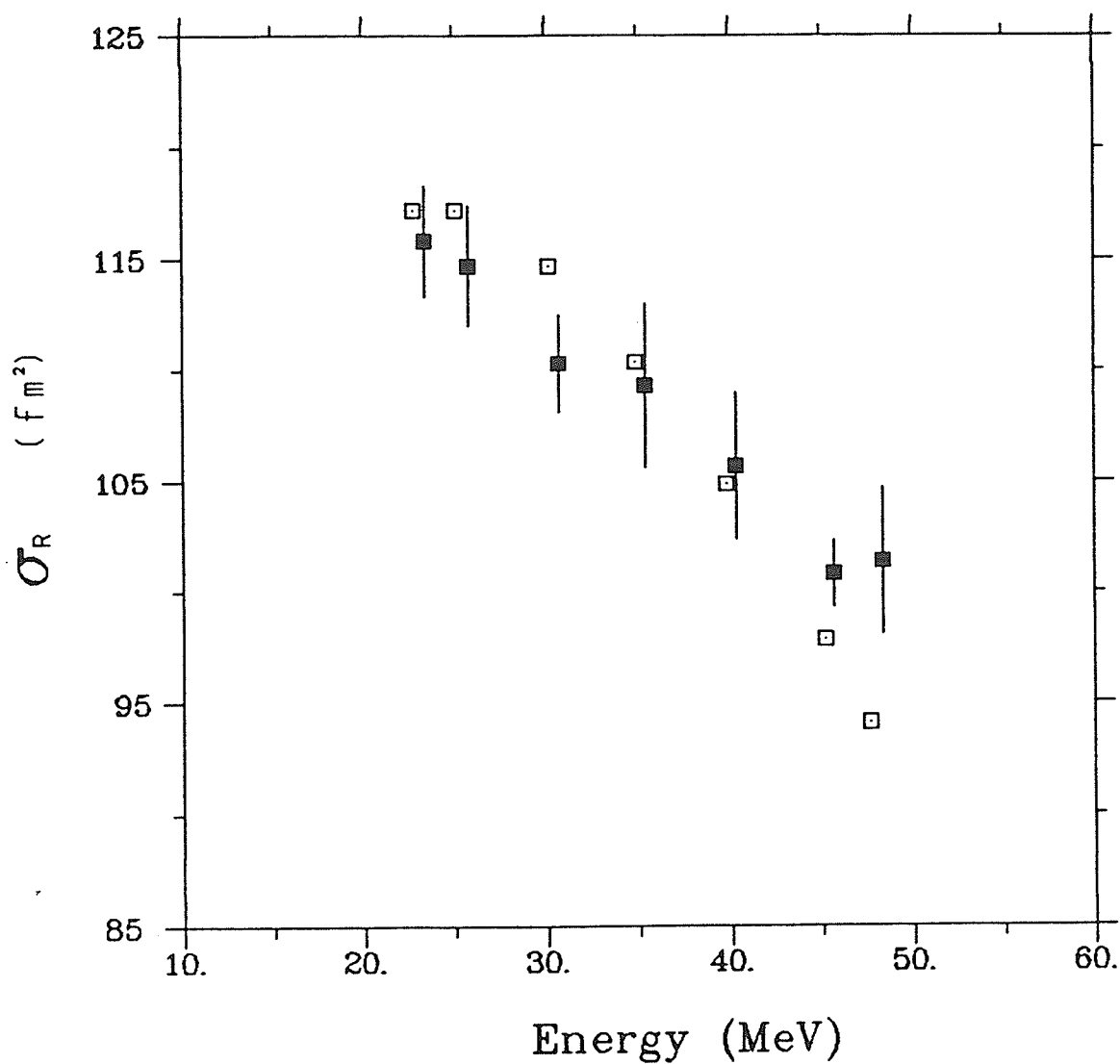


[Fig. 13]

Total reaction cross sections for $p+\text{Ni}^{60}$ using the non-relativistic optical model with global parameters: ■, $\sigma_R(\text{Exp})$; □, $g^l \sigma_R(\text{Theo})$.

[Table 9]

Relativistic Optical Model Parameters for $p+Ni^{60}$

Energy (MeV)	V_V (MeV)	R_V^1 (fm)	A_V^1 (fm)	W_V (MeV)	R_V^2 (fm)	A_V^2 (fm)	V_S (MeV)	R_S^1 (fm)	A_S^1 (fm)	W_S (MeV)	R_S^2 (fm)	A_S^2 (fm)	χ^2	$\sigma_R(\text{Theo})$ (fm ²)	$\sigma_R(\text{Exp})$ (fm ²)
18.6	248.7	1.040	0.652	-10.82	1.421	0.412	-314.7	1.075	0.682	4.14	1.025	0.412	5.8	113.2	
30.3	249.2	1.045	0.653	-10.82	1.420	0.412	-313.9	1.068	0.681	4.14	1.025	0.412	31.5	110.3	110.3±2.2
35.2	249.3	1.047	0.653	-10.82	1.420	0.412	-313.7	1.066	0.681	4.14	1.025	0.412	25.8	107.0	109.3±3.7
40.0	249.3	1.047	0.653	-10.82	1.419	0.412	-313.7	1.066	0.681	4.14	1.025	0.412	20.3	105.4	105.7±3.3
55.0	263.5	1.046	0.654	-9.49	1.412	0.411	-324.8	1.065	0.678	4.18	1.026	0.412	4.6	91.2	
65.7	276.3	1.053	0.653	-9.28	1.412	0.411	-345.9	1.059	0.680	4.23	1.026	0.412	283.0	85.0	

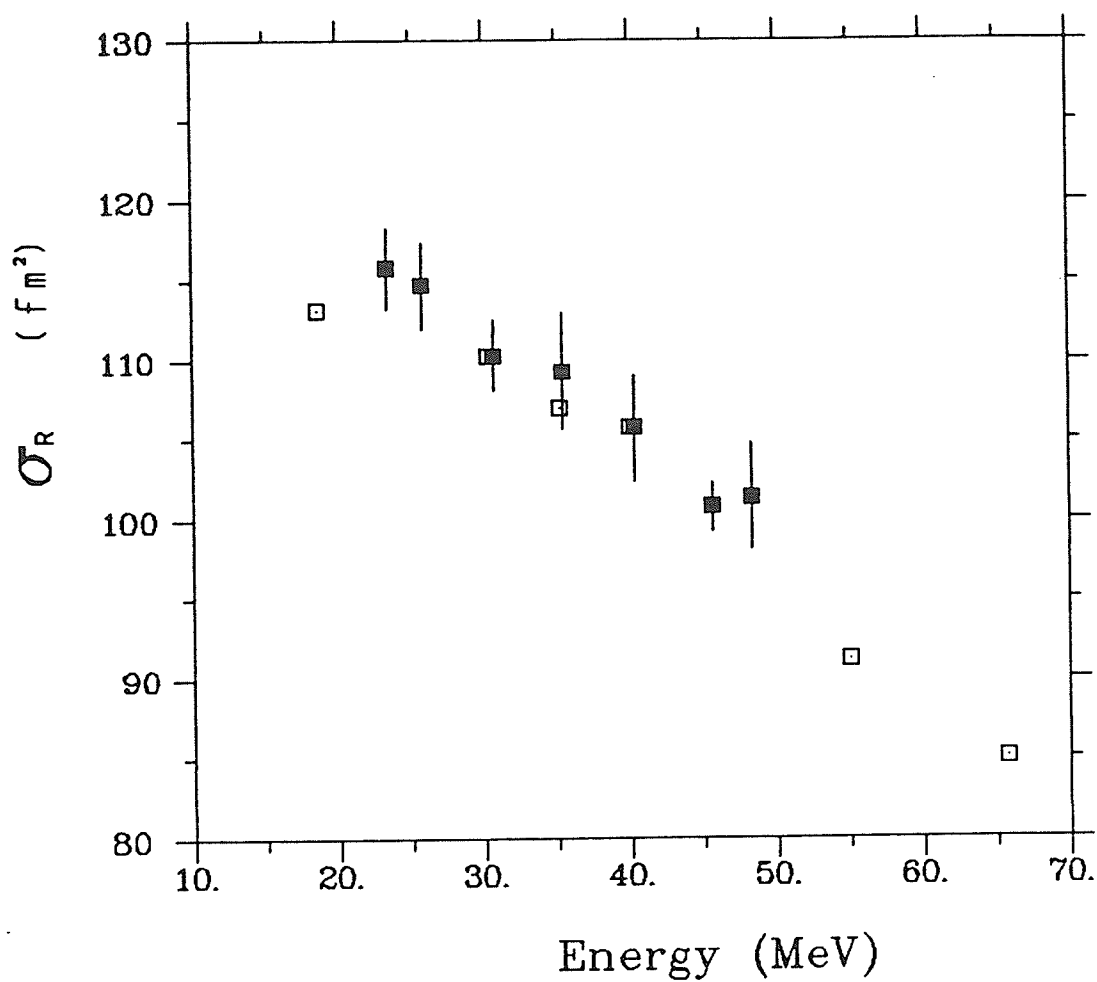


[Fig. 14]

Total reaction cross sections for $p+\text{Ni}^{60}$ using the relativistic optical model: \blacksquare , $\sigma_R(\text{Exp})$; \square , $\sigma_R(\text{Theo})$.

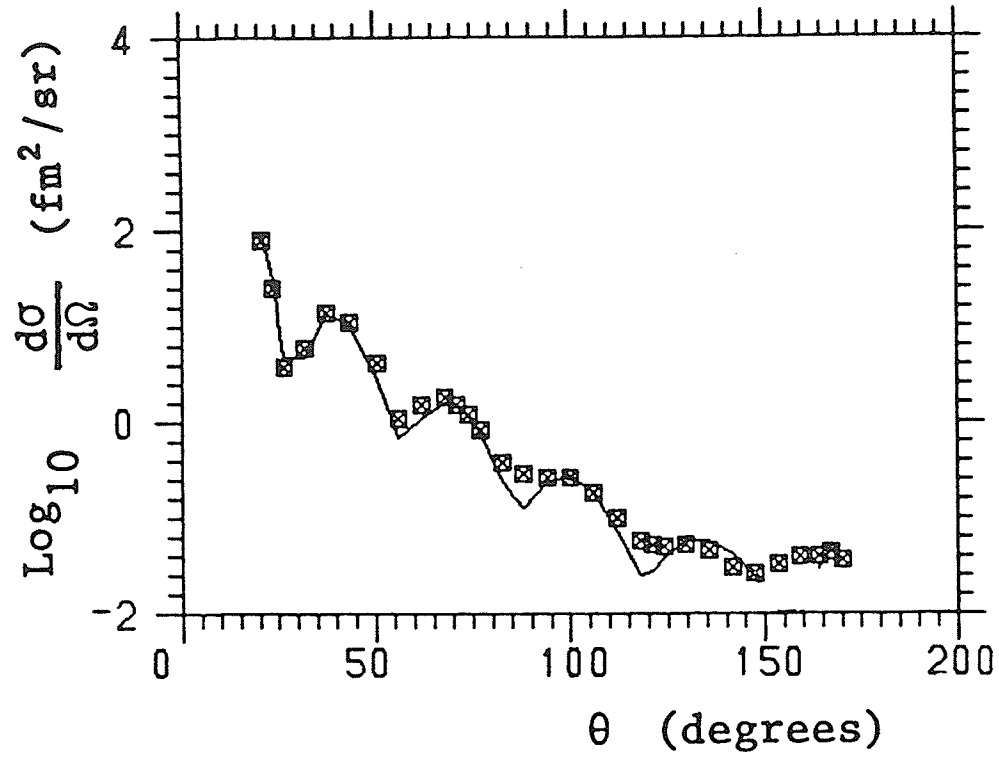


[Fig. 15]

Best fit differential cross sections for $p+\text{Ni}^{60}$
at 35 MeV using the relativistic optical model.

Total reaction cross section values obtained from the relativistic optical model analysis are listed in [Table 9] together with the potential parameters. Chisquare values and experimental reaction cross section values at each energy are presented in [Table 9] as well. Experimental reaction cross sections for Ni⁶⁰ have been plotted in [Fig. 14] along with the total reaction cross section predictions extracted from the Dirac equation based model. The agreement is quite remarkable. A sample fit to the differential cross section at 35 MeV is presented in [Fig. 15]. Although the large angle discrepancy was again observed at angles larger than approximately about 90^o, in several other relativistic model analyses in the low energy range [Ref. 29, 31], remarkable agreement was obtained with large angle data, while non-relativistic analyses require an additional term in the optical model which depends on the orbital angular momentum to obtain such agreement.

IV.3. CALCIUM-48

Total reaction cross section values for Ca⁴⁸ are presented in [Table 10] along with the associated corrections. Again, the main contribution to the correction of the uncorrected reaction cross section was from the elastic correction. [Fig. 16] shows the variation of σ_R with energy. The smooth decrease of σ_R with increasing proton energy, with no dips and enhancements, was observed over the energy range under study.

[Table 10]

Proton Total Reaction Cross Sections for Ca⁴⁸

Energy (MeV)	σ_{un} (fm ²)	Elastic correct. (fm ²)	Large angle charged part. correction (8°-45°) (fm ²)	Small angle charged part. correction (0°-8°) (fm ²)	Correction for react. in the stopping detector (fm ²)	Correction for react. in detector 5 (fm ²)	σ_R (fm ²)
23.0	121.5±3.9	15.2±1.4	0.8±0.2	0.6±0.3	1.5±0.1	0.2±0.1	106.3±4.1
25.3	119.9±4.5	13.9±0.7	0.9±0.2	0.6±0.3	1.5±0.1	0.1±0.1	105.7±4.6
30.3	111.8±5.4	11.3±0.6	1.0±0.2	0.7±0.3	2.2±0.4	0.1±0.1	99.9±5.5
35.1	106.5±3.1	8.9±0.4	1.0±0.2	0.7±0.3	2.1±0.3	0.1±0.1	96.9±3.1
40.0	102.4±2.9	6.6±0.3	0.9±0.2	0.7±0.3	2.5±0.4	0.1±0.1	95.0±3.1
45.3	97.2±3.7	4.2±0.2	0.8±0.2	0.6±0.3	2.6±0.5	0.1±0.1	91.3±3.9
48.0	92.7±2.8	3.1±0.2	0.6±0.1	0.6±0.3	2.4±0.5	0.1±0.1	88.5±2.8

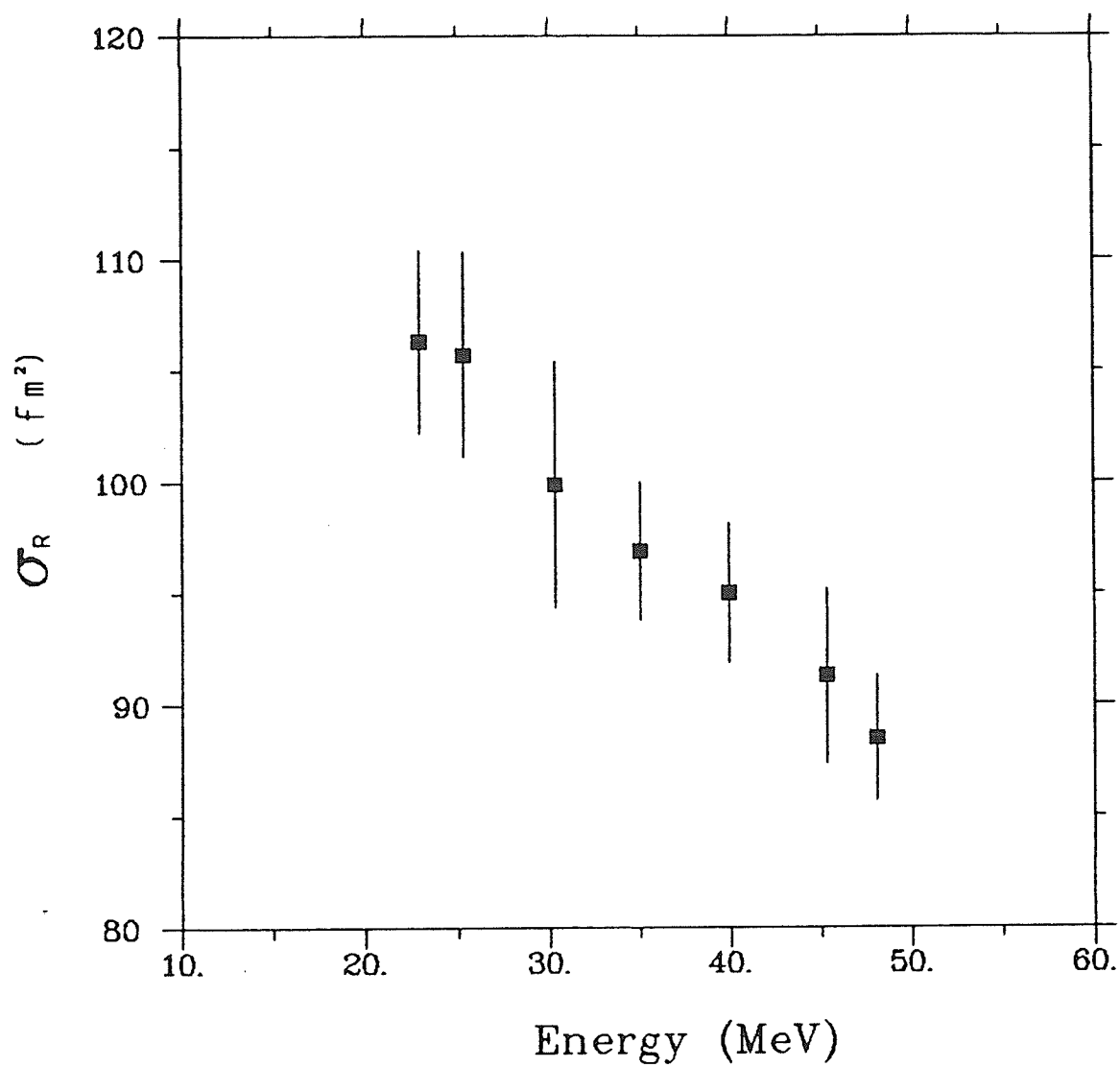


[Fig. 16]

$p+\text{Ca}^{40}$ total reaction cross sections:

■, present work.

Transparency calculations were completed for Ca^{48} ; with the choice of radius parameter, $r_o = 1.56$ fm, the maximum transparency, on the order of 21.45%, occurred at 48 MeV incident proton energy, while minimum transparency was observed at 23.0 MeV. The results are presented in [Table 11]. $\sigma_R(\text{Exp})$ and $\sigma_R(\text{bl})$ values are plotted as a function of incoming proton energy in [Fig. 17]. The increasing difference between $\sigma_R(\text{Exp})$ and $\sigma_R(\text{bl})$ values at energies, above approximately, 35 MeV is attributed to an increase (from zero) of the nuclear transparency T .

A non-relativistic optical model analysis with global parameters was performed for this nucleus. The global potential parameters and total reaction cross section predictions, $g^1\sigma_R(\text{theo})$, are presented in [Table 12] along with the experimental total reaction cross section, $\sigma_R(\text{Exp})$, values. $\sigma_R(\text{Exp})$ and $g^1\sigma_R(\text{theo})$ values are plotted as a function of proton energy in [Fig. 18]. A comparison was also made with the reaction cross section values, ${}^{\text{op}}\sigma_R(\text{theo})$, obtained from the non-relativistic optical model analysis for $p\text{-Ca}^{48}$ elastic scattering [Ref. 31] in [Fig. 19]. The increasing difference between $\sigma_R(\text{Exp})$ and $g^1\sigma_R(\text{theo.})$ values with decreasing energy, up to 20% at 23 MeV, is attributed to the closed-shell effects of the doubly-magic Ca^{48} nucleus. Although, the ${}^{\text{op}}\sigma_R(\text{theo})$ predictions have higher values than the $\sigma_R(\text{Exp})$ results, the standard non-relativistic optical model gives slightly better agreement than the optical model with global parameters.

[Table 11]

Nuclear Transparency Calculations for Ca^{48}

r_0 (fm)	Energy (MeV)	$\sigma_R(\text{Exp})$ (fm ²)	$\sigma_R(\text{bl})$ (fm ²)	T (%)
1.56	48.0	88.5±2.8	112	21
	45.3	91.3±3.9	112	18
	40.0	95.0±3.1	111	15
	35.1	96.9±3.1	111	12
	30.3	99.9±5.5	110	9
	25.3	105.7±4.6	108	2
	23.0	106.3±4.1	106	0

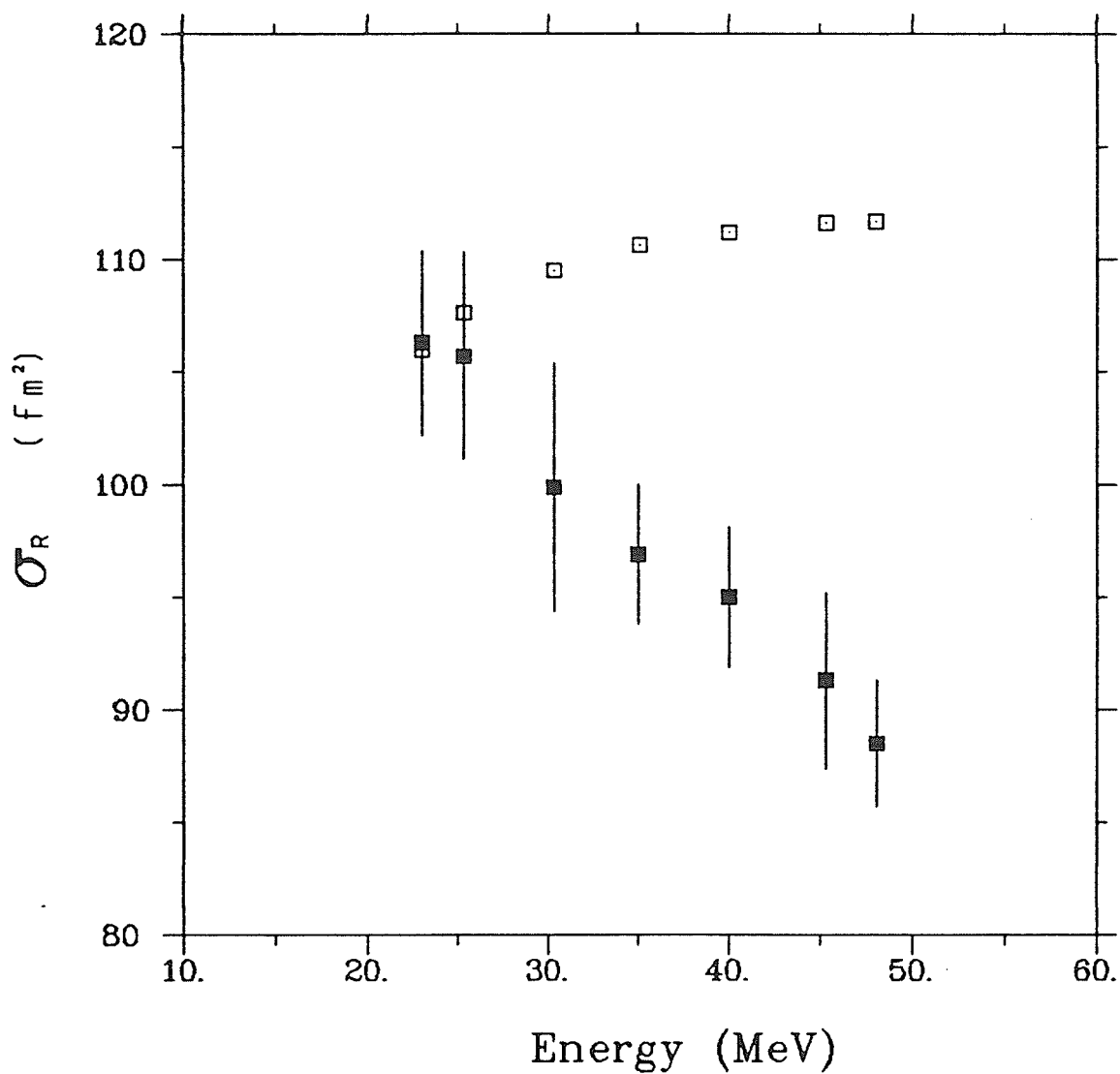


[Fig. 17]

The results of the nuclear transparency calculations
for $p+\text{Ca}^{40}$: \blacksquare , $\sigma_R(\text{Exp})$; \square , $\sigma_R(\text{bl})$.

[Table 12]

Non-Relativistic Optical Model Parameters for p+Ca⁴⁰

Energy (MeV)	V (MeV)	a ₀ (fm)	r ₀ (fm)	W _{sf} (MeV)	a ₁ (fm)	r ₁ (fm)	W _{so} (MeV)	V _{so} (MeV)	a _{so} (fm)	r _{so} (fm)	σ_R^L (Theo) (fm ²)	σ_R (Exp) (fm ²)
22.97	52.85	0.75	1.17	8.06	0.63	1.32	2.35	6.20	0.75	1.01	123.1	106.3±4.1
25.30	52.10	0.75	1.17	7.48	0.63	1.32	2.87	6.20	0.75	1.01	121.8	105.7±4.6
30.29	50.51	0.75	1.17	6.23	0.63	1.32	3.96	6.20	0.75	1.01	112.5	99.9±5.5
35.02	48.99	0.75	1.17	5.05	0.63	1.32	5.00	6.20	0.75	1.01	117.6	96.9±3.1
39.93	47.42	0.75	1.17	3.82	0.63	1.32	6.08	6.20	0.75	1.01	106.4	95.0±3.1
45.28	45.71	0.75	1.17	2.48	0.63	1.32	7.26	6.20	0.75	1.01	99.2	91.3±3.9
47.99	44.84	0.75	1.17	1.81	0.63	1.32	7.86	6.20	0.75	1.01	95.3	88.5±2.8

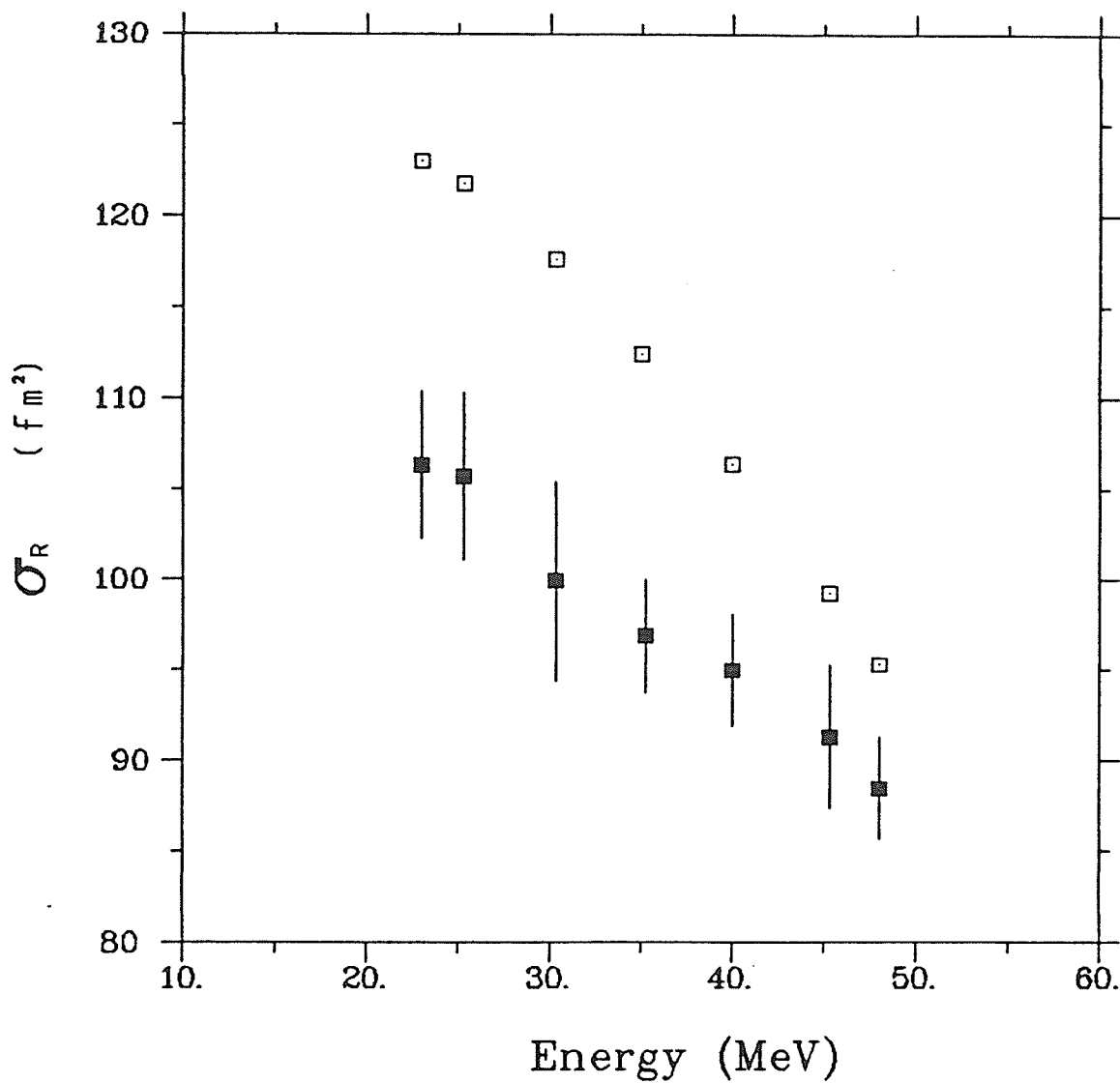


[Fig. 18]

Total reaction cross sections for $p+\text{Ca}^{48}$ using the non-relativistic optical model with global parameters: \blacksquare , σ_R (Exp); \square , $g^{\lambda} \sigma_R$ (Theo).

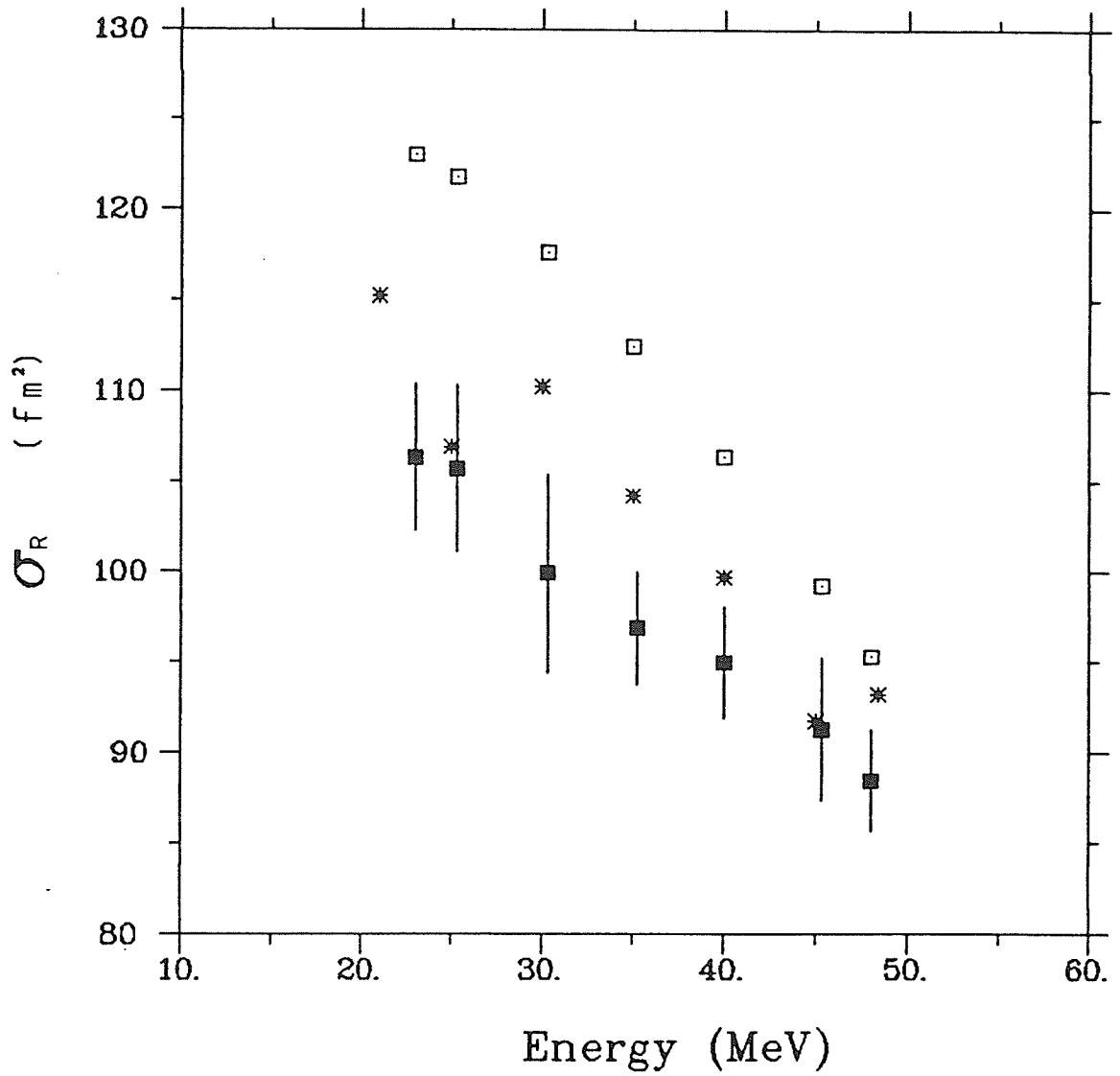


[Fig. 19]

Comparison of Ca^{*0} results with the non-relativistic optical model predictions and optical model calculations with global parameters: \blacksquare , σ_R (Exp); \square , $g^l \sigma_R$ (Theo); $*$, $^{op} \sigma_R$ (Theo).

The total reaction cross section for Ca^{48} are plotted in [Fig. 20] along with the relativistic optical model predictions obtained from [Ref. 31] for $p+\text{Ca}^{48}$ elastic scattering. The agreement between the experimental and predicted reaction cross sections was quite remarkable. Potential parameters are also presented in [Table 13].

[Table 13]

Relativistic Optical Model Parameters for $p+Ca^{40}$

Energy (MeV)	V_V (MeV)	R_V^1 (fm)	A_V^1 (fm)	W_V (MeV)	R_V^2 (fm)	A_V^2 (fm)	V_S (MeV)	R_S^1 (fm)	A_S^1 (fm)	W_S (MeV)	R_S^2 (fm)	A_S^2 (fm)	χ^2	$\sigma_R(\text{Theo})$ (fm ²)	$\sigma_R(\text{EXP})$ (fm ²)
21.0	428.2	0.952	0.612	-11.18	1.592	0.580	-565.0	0.929	0.667	96.08	0.877	1.127	9.7	106.4	
25.0	514.1	0.991	1.060	-10.19	1.601	0.388	-651.4	0.966	1.028	15.26	0.871	0.569	4.1	103.5	105.7±4.6
30.0	438.2	0.899	0.900	-6.36	1.698	0.344	-537.0	0.914	0.876	8.68	0.929	0.092	18.8	98.6	99.9±5.5
35.0	387.1	0.973	0.867	-6.25	1.669	0.396	-482.3	0.979	0.843	6.40	0.943	0.024	18.9	95.9	96.9±3.1
40.0	388.6	1.007	0.857	-6.55	1.609	0.418	-490.0	1.004	0.840	2.15	0.911	0.028	25.0	94.7	95.0±3.1
45.0	358.1	0.922	0.837	-6.87	1.559	0.454	-445.7	0.945	0.816	3.26	0.882	0.002	32.6	90.3	91.3±3.9
48.4	443.0	0.987	0.684	-9.51	1.490	0.412	-581.0	0.967	0.709	4.18	1.079	0.043	9.7	89.0	88.5±2.8

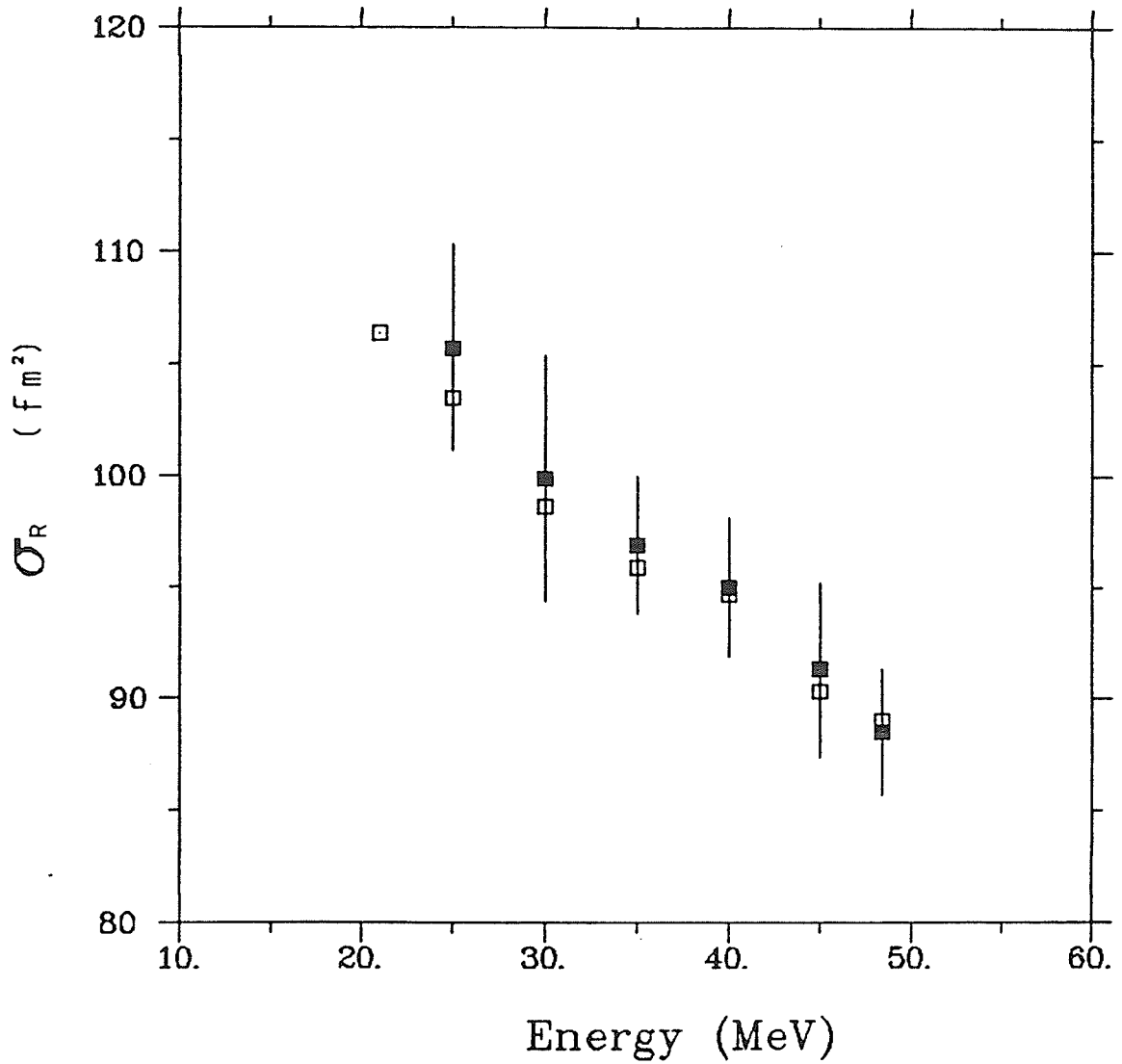


[Fig. 20]

Total reaction cross sections for $p+\text{Ca}^{48}$ using the relativistic optical model: \blacksquare , $\sigma_R(\text{Exp})$; \square , $\sigma_R(\text{Theo})$.

IV.4. SUMMARY

In this experiment, total reaction cross sections have been measured for the nuclei Ni^{58} , Ni^{60} and Ca^{48} between 23 and 48 MeV. The accuracy of the measured cross sections was between 1 and 3% for Ni^{58} and Ni^{60} and 2 to 5% for Ca^{48} . The uncertainties associated with the uncorrected cross sections are due to statistical fluctuations in the measurements of the reaction rates with the target in and out. Reproducibility of the data was checked by making three or more measurements for each target at each energy.

The general feature of the reaction cross sections is a smooth decrease with increasing incident proton energy. The optical model predictions of σ_R , with global parameters, obtained using the modified version of program SEEK for Ni^{58} , Ni^{60} are in good agreement with the measured values in the energy range under study, but are up to 20% higher than the experimental reaction cross sections for Ca^{48} . The error in the calculated reaction cross section using the optical model with global parameters is estimated to be $\pm 10\%$.

The nuclear transparency results were calculated using the radius parameters $r_0 = 1.53, 1.55$ fm for Ni^{58} and Ni^{60} , respectively, and $r_0 = 1.56$ fm for Ca^{48} . The minimum transparency T was observed at about 20 to 25 MeV for each nucleus.

[Fig. 21] displays the reaction cross sections divided by $A^{2/3}$ and plotted versus the neutron number for the nuclei from Si^{28} to Zn^{68} , [Ref. 45] together with the present measurements, at 24.8, 34.8 and 44.8 MeV. On the average, there is a slight decrease in $\sigma_R A^{-2/3}$ as a function of increasing neutron number for 24.8 and 34.8 MeV incident protons. In addition, there is a dip in $\sigma_R A^{-2/3}$ at $N=28$, and the value for Ca^{40} (doubly magic nucleus $N=Z=20$) is lower than for nearby nuclei. Finally, it is observed that for the isotopic sequences for Ca, Fe and Ni, there is an increase in $\sigma_R A^{-2/3}$ as N increases, with the exception of the doubly magic Ca^{48} .

Reaction cross section predictions were extracted from the Dirac equation based optical model analyses for Ni^{58} , Ni^{60} and Ca^{48} in the energy range under study. Calculated and experimental σ_R results are in very good agreement for each target nucleus. The relativistic approach, in particular, gave a better representation than non-relativistic approaches for Ca^{48} reaction cross section predictions.

[Figs. 22, 23, 24] summarize all the calculated and measured reaction cross section values for Ni^{58} , Ni^{60} and Ca^{48} in the energy range under study.

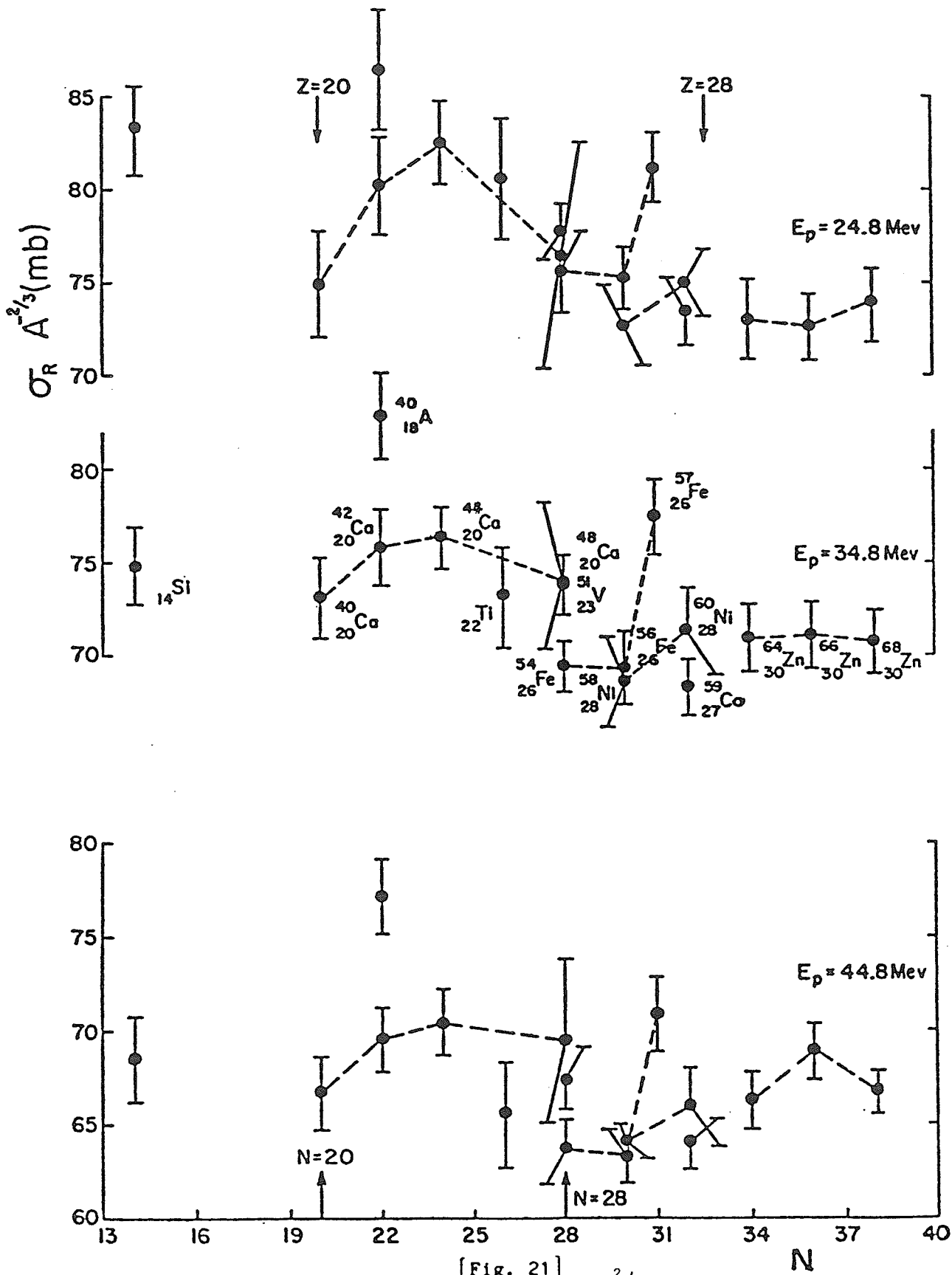


[Fig. 21] The reaction cross sections divided by $A^{2/3}$ and plotted versus the neutron number for the nuclei from Si^{28} to Zn^{68} .

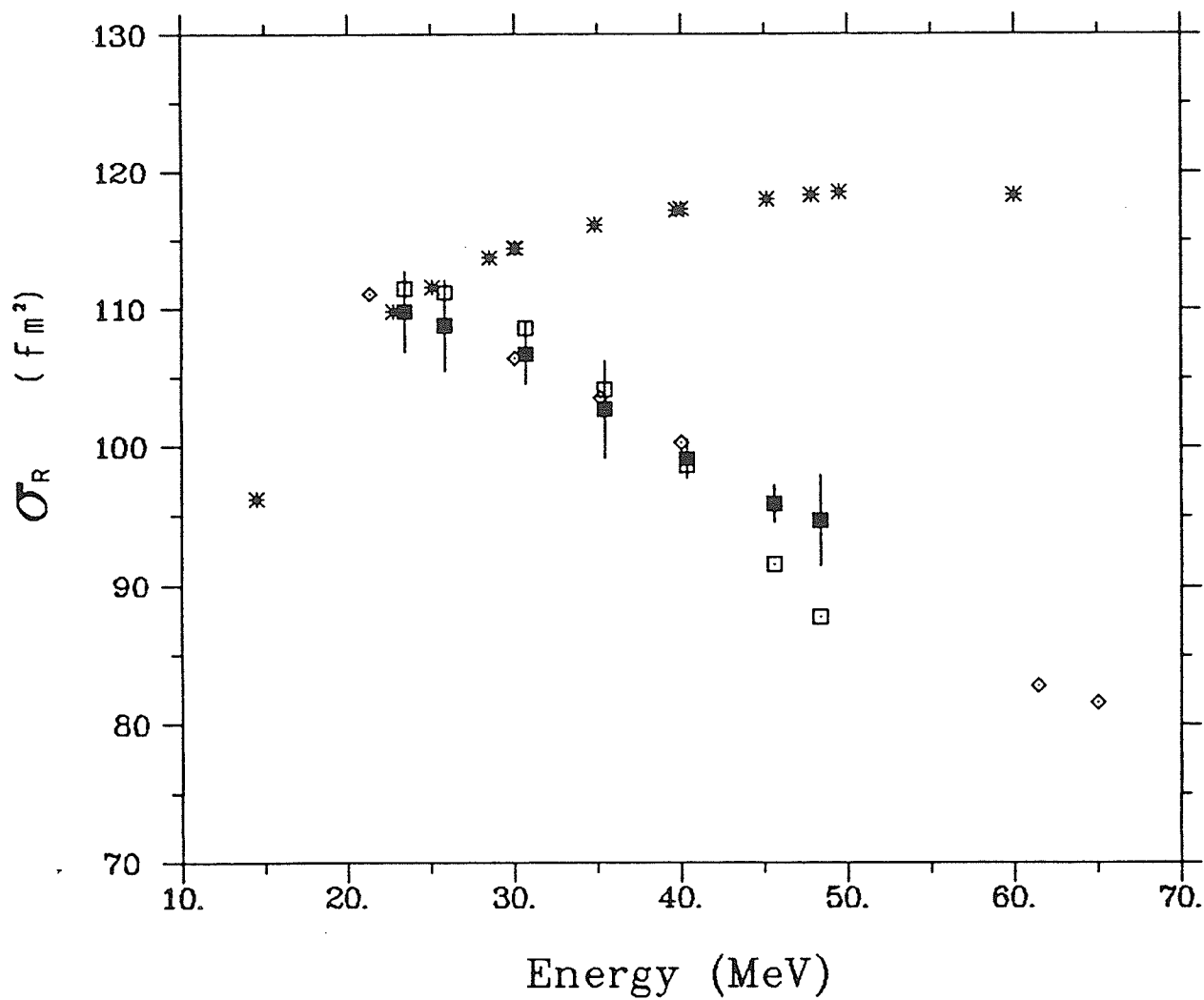


[Fig. 22]

The calculated and measured total reaction cross section values for Ni^{50} : ■, $\sigma_R(\text{Exp})$; *, $\sigma_R(\text{bl})$; □, $g^l \sigma_R(\text{Theo})$; ◇, $\sigma_R(\text{Theo})$ using the relativistic optical model.

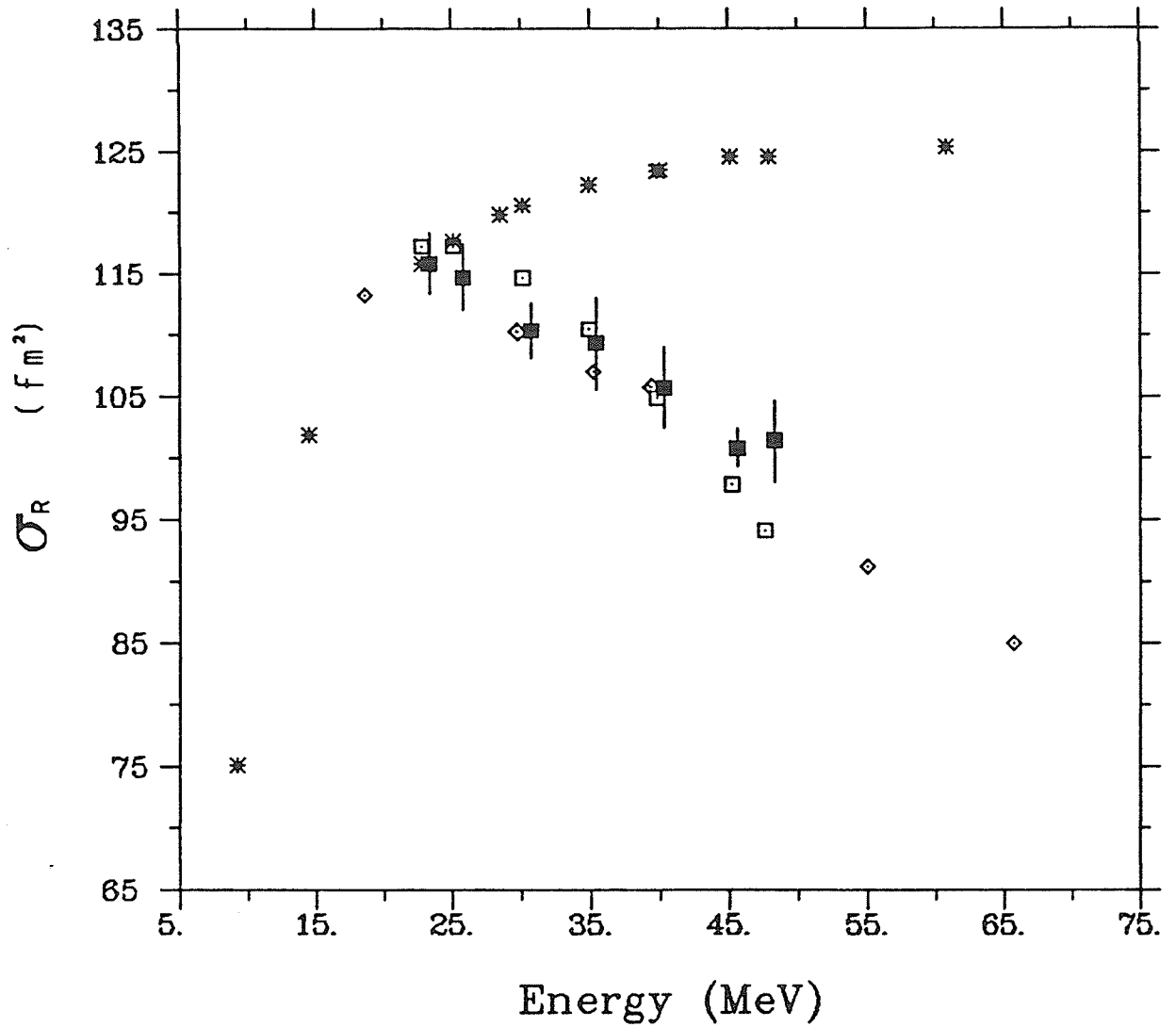


[Fig. 23]

The calculated and measured total reaction cross section values for Ni^{60} : ■, $\sigma_R(\text{Exp})$; *, $\sigma_R(\text{bl})$; □, $\sigma_R^{\text{gl}}(\text{Theo})$; ◇, $\sigma_R(\text{Theo})$ using the relativistic optical model.

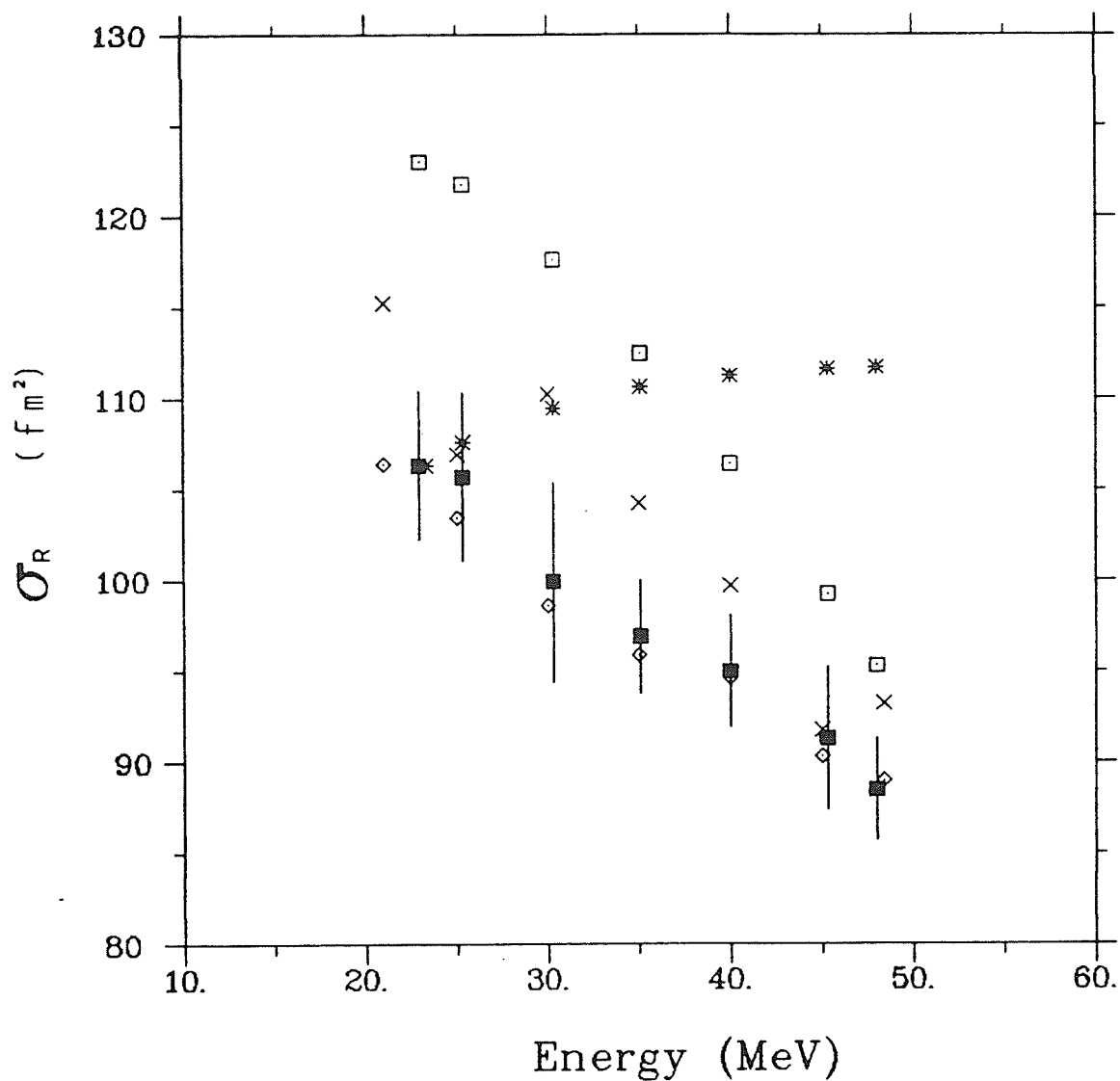


[Fig. 24]

The calculated and measured total reaction cross section values for Ca^{40} : ■, $\sigma_R(\text{Exp})$; *, $\sigma_R(\text{bl})$; □, $^{gl}\sigma_R(\text{Theo})$; x, $^{op}\sigma_R(\text{Theo})$; ◆, $\sigma_R(\text{Theo})$ using the relativistic optical model.

REFERENCES

1. B. Buck, Phys. Rev. 130, 712 (1963)
2. L. Rosen, J. G. Beery, A. S. Goldhaber and E. H. Auerbach, Ann. Phys. (N.Y.) 34, 96 (1965).
3. M. P. Fricke, E. E. Gross, B. J. Morton and A. Zucker, Phys. Rev. 156, 1207 (1967)
4. F. D. Becchetti and G. W. Greenlees, Phys. Rev. 182, 1190 (1969)
5. I. H. Sloan, Nucl. Phys. A168, 211 (1971)
6. J. F. Dicello, G. J. Igo and M. L. Roush, Phys. Rev. 157, 1001 (1967)
7. J. J. H. Menet, E. E. Gross, J. J. Malanify, and A. Zucker, Phys. Rev. C4, 1114 (1971)
8. J. F. Turner, B. W. Ridley, P. E. Cavanagh, G. A. Gard and A. E. Hardacre, Nucl. Phys. 58, 509 (1964)
9. B. D. Wilkins and G. J. Igo, Phys. Rev. 129, 2198 (1963)
10. R. E. Pollock and G. Schrank, Phys. Rev. 140, B575 (1965)
11. M. Q. Makino, C. N. Waddell and R. M. Eisberg, Nucl. Phys. 68, 378 (1965)
12. R. Goloskie and K. Strauch, Nucl. Phys. 29, 474 (1962)
13. K. Bearpark, W. R. Graham and G. Jones, Nucl. Phys. 73, 206 (1965)
14. P. J. Bulman and J. A. R. Griffith, Nucl. Phys. A111, 315 (1968)
15. P. U. Renberg, D.F. Measday, M. Pepin et al., Nucl. Phys. A183, 81 (1972)
16. R. M. De Vries and J. C. Peng, Phys. Rev. C22, 1055 (1980)
17. R. F. Carlson, A. J. Cox, T. N. Nasr et al., Nucl. Phys. A445, 57 (1985)
18. H. Duerr, Phys. Rev. 103, 469 (1956)
19. M. H. Johnson and E. Teller, Phys. Rev. 98, 783 (1955)

20. L. D. Miller and A. E. S. Green, Phys. Rev. C5, 241 (1972)
21. R. Brockmann, Phys. Rev. C18, 1510 (1978)
22. J. D. Walecka, Ann. Phys. (N.Y.) 83, 491 (1974)
23. S. A. Chin, Ann. Phys. (N.Y.) 108, 301 (1977)
24. R. L. Mercer, L. G. Arnold and B. C. Clark, Phys. Lett. 73B, 9 (1978)
25. L. G. Arnold and B. C. Clark, Phys. Lett. 84B, 46 (1979)
26. L. G. Arnold, B. C. Clark and R. L. Mercer, Phys. Rev. C19, 917 (1979)
27. L. G. Arnold, B. C. Clark, R. L. Mercer and P. Schwandt,
Phys. Rev. C23, 1949 (1981)
28. L. G. Arnold, B. C. Clark, R. L. Mercer and P. Schwandt,
Phys. Rev. C23, 15 (1981)
29. B. C. Clark, S. Hama and R. L. Mercer, in The Interaction between Medium
Energy Nucleons in Nuclei - 1982 ed. by H. O. Meyer A. I. P. Conference
Proceedings No. 97 p. 260
30. B. C. Clark, Invited Talk Presented at the Bates Users Theory Group
Meeting - Aug 9, 1985 (Unpublished)
31. R. H. McCamis, T. N. Nasr et al., Phys. Rev. C33, 1624 (1986)
32. R. F. Carlson, W. F. McGill, T. H. Short et al.,
Nucl. Instr. Meth. 123, 509 (1975)
33. W. F. McGill, R. F. Carlson, T. H. Short et al.,
Phys. Rev. C10, 2237 (1974)
34. T. N. Nasr, M.Sc. thesis, University of Manitoba - May, 1977
35. O. N. Jarvis et al., Nucl. Phys. A102, 625 (1967)
36. S. F. Eccles et al., Phys. Rev. 141, 1067 (1966)
37. N. Baron et al., Phys. Rev. 180, 978 (1969)

38. H. S. Liers et al., Phys. Rev. C2, 1399 (1970)
39. E. Febrici, S. Micheletti, M. Pignanelli et al., Phys. Rev. C21, 844 (1980)
40. C. B. Fulmer et al., Phys. Lett. 24B, 505 (1967)
41. M. Koike, K. Matsu et al., J. Phys. Soc. Japan 21, 2103 (1966)
42. O. Karban et al., Nucl. Phys. A147, 461 (1970)
43. M. P. Fricke, E. E. Gross and A. Zucker, Phys. Rev. 163, 1153 (1967)
44. D. W. Devins et al., Nucl. Phys. 35, 617 (1962)
45. R. F. Carlson, Private Communications
46. H. Sakaguchi, M. Nakamura, K. Hatanaka et al., Phys. Rev. C26, 944 (1982)
47. L. G. Arnold, B. C. Clark and R. L. Mercer, Phys. Rev. C21, 1899 (1980)
48. C. J. Horowitz, Phys. Rev. C31, 1340 (1984)
49. H. Bichsel and C. Tschalaer, Nucl. Data A3, 343 (1967)
50. H. Bichsel and C. Tschalaer, UCRL-17663, Rev. 1 (1968)
51. R. Hofstadter, Electron Scattering and Nuclear and Nucleon Structure,
1963 ed. by W. A. Benjamin Inc. p. 220